

Today's outline - November 02, 2021





- *In situ* studies of methanol fuel cells

Today's outline - November 02, 2021



- *In situ* studies of methanol fuel cells
- Reversibility in tin-based anode materials

Today's outline - November 02, 2021



- *In situ* studies of methanol fuel cells
- Reversibility in tin-based anode materials
- Angle Resolved Photoemission

Today's outline - November 02, 2021



- *In situ* studies of methanol fuel cells
- Reversibility in tin-based anode materials
- Angle Resolved Photoemission
- HAXPES

Today's outline - November 02, 2021



- *In situ* studies of methanol fuel cells
- Reversibility in tin-based anode materials
- Angle Resolved Photoemission
- HAXPES

Reading Assignment: Chapter 8.1–8.3



- *In situ* studies of methanol fuel cells
- Reversibility in tin-based anode materials
- Angle Resolved Photoemission
- HAXPES

Reading Assignment: Chapter 8.1–8.3

Homework Assignment #06:

Chapter 6: 1,6,7,8,9

due Tuesday, November 16, 2021



- *In situ* studies of methanol fuel cells
- Reversibility in tin-based anode materials
- Angle Resolved Photoemission
- HAXPES

Reading Assignment: Chapter 8.1–8.3

Homework Assignment #06:

Chapter 6: 1,6,7,8,9

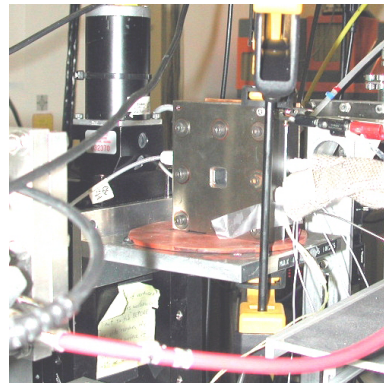
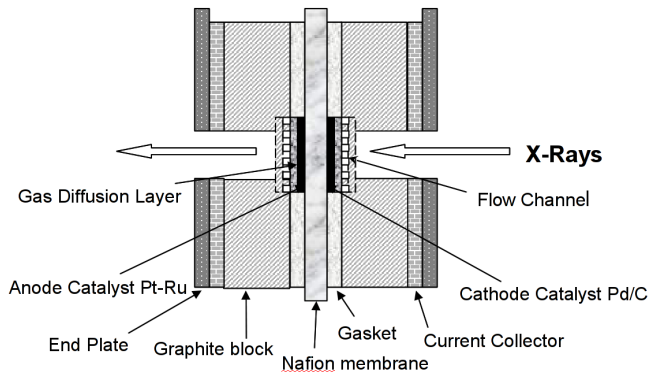
due Tuesday, November 16, 2021

Homework Assignment #07:

Chapter 7: 2,3,9,10,11

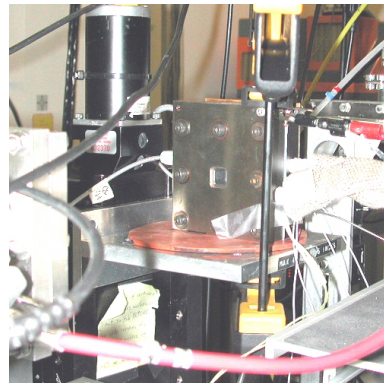
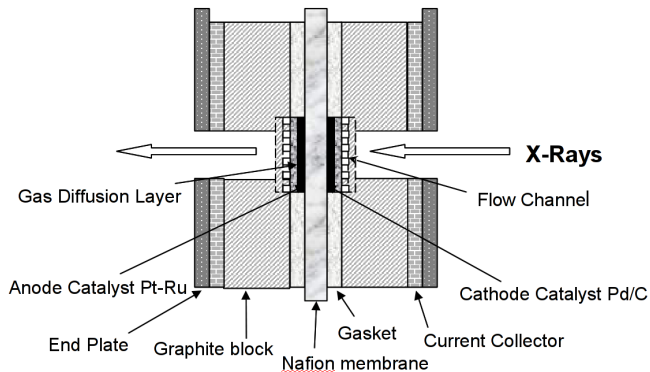
due Tuesday, November 30, 2021

Mark I operando fuel cell



R. Viswanathan et al., "In-situ XANES study of carbon supported Pt-Ru anode electrocatalysts for reformat-air polymer electrolyte fuel cells," *J. Phys. Chem. B* **106**, 3458 (2002).

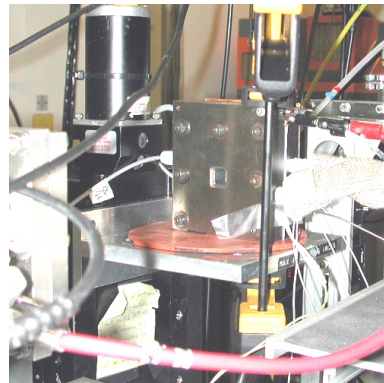
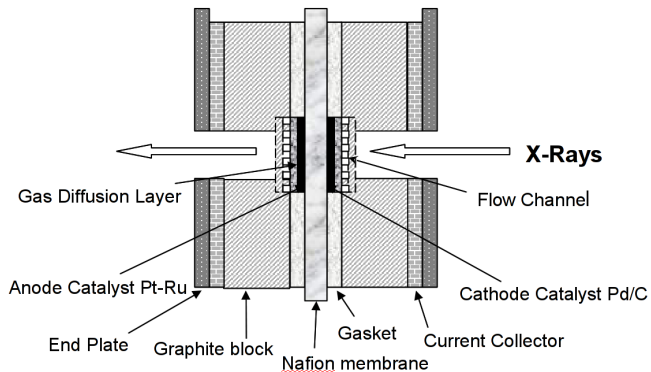
Mark I operando fuel cell



- Transmission mode

R. Viswanathan et al., "In-situ XANES study of carbon supported Pt-Ru anode electrocatalysts for reformat-air polymer electrolyte fuel cells," *J. Phys. Chem. B* **106**, 3458 (2002).

Mark I operando fuel cell

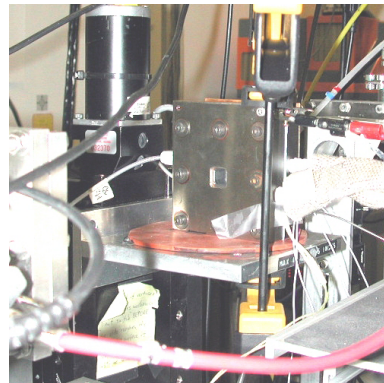
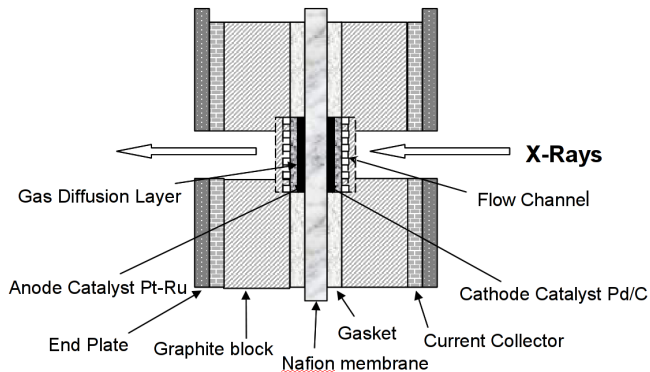


- Transmission mode

- < 1 mm of graphite

R. Viswanathan et al., "In-situ XANES study of carbon supported Pt-Ru anode electrocatalysts for reformat-air polymer electrolyte fuel cells," *J. Phys. Chem. B* **106**, 3458 (2002).

Mark I operando fuel cell

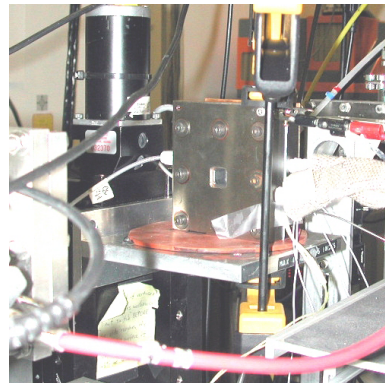
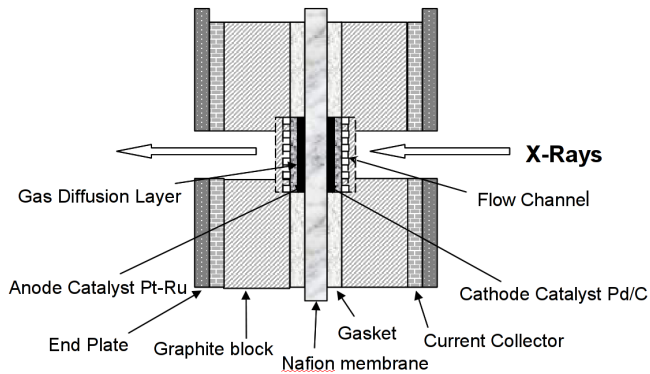


- Transmission mode
- Pt/Ru on anode

- <1 mm of graphite

R. Viswanathan et al., "In-situ XANES study of carbon supported Pt-Ru anode electrocatalysts for reformat-air polymer electrolyte fuel cells," *J. Phys. Chem. B* **106**, 3458 (2002).

Mark I operando fuel cell

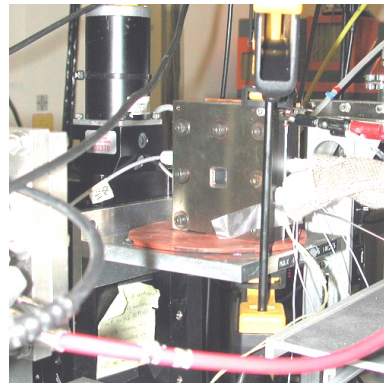
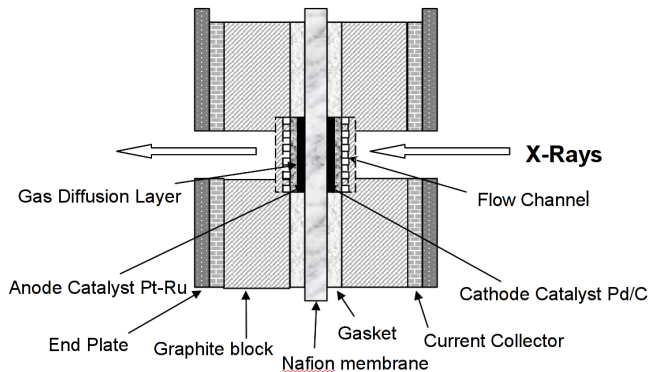


- Transmission mode
- Pt/Ru on anode

- <1 mm of graphite
- Pd on cathode

R. Viswanathan et al., "In-situ XANES study of carbon supported Pt-Ru anode electrocatalysts for reformat-air polymer electrolyte fuel cells," *J. Phys. Chem. B* **106**, 3458 (2002).

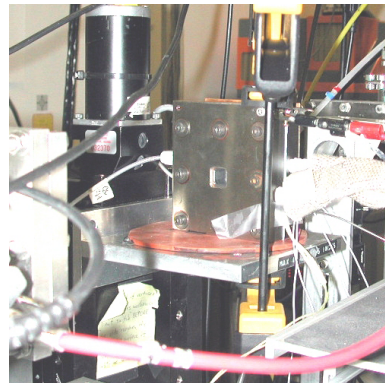
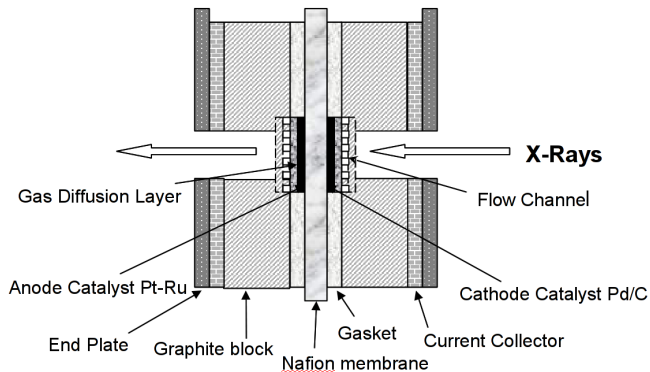
Mark I operando fuel cell



- Transmission mode
- Pt/Ru on anode
- 35°C operating temp
- <1 mm of graphite
- Pd on cathode

R. Viswanathan et al., "In-situ XANES study of carbon supported Pt-Ru anode electrocatalysts for reformat-air polymer electrolyte fuel cells," *J. Phys. Chem. B* **106**, 3458 (2002).

Mark I operando fuel cell

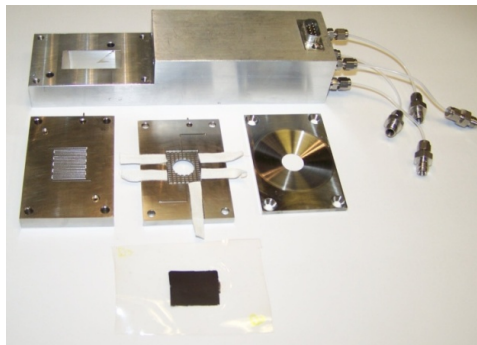
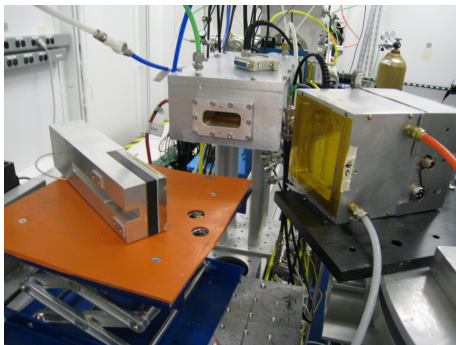


- Transmission mode
- Pt/Ru on anode
- 35°C operating temp

- <1 mm of graphite
- Pd on cathode
- 1-2 min scan time

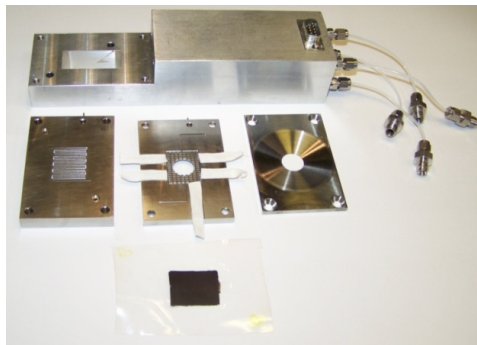
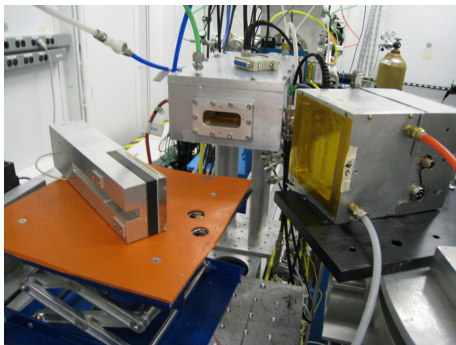
R. Viswanathan et al., "In-situ XANES study of carbon supported Pt-Ru anode electrocatalysts for reformat-air polymer electrolyte fuel cells," *J. Phys. Chem. B* **106**, 3458 (2002).

Mark II operando fuel cell



E.A. Lewis et al., "Operando x-ray absorption and infrared fuel cell spectroscopy", *Electrochim. Acta.* **56**, 8827 (2011).

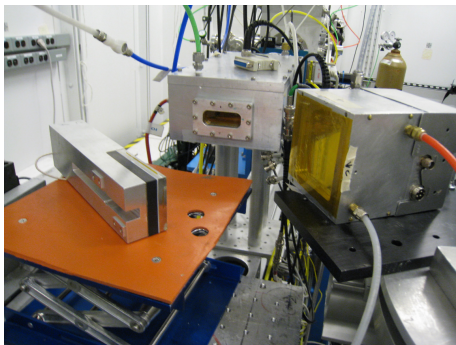
Mark II operando fuel cell



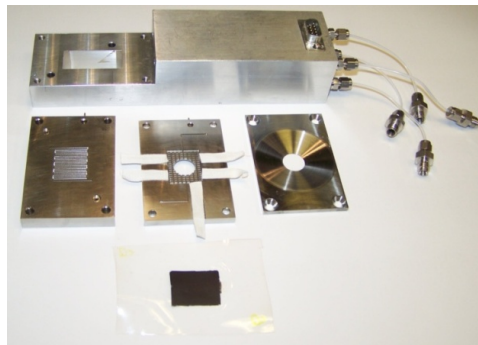
- Air-breathing cathode

E.A. Lewis et al., "Operando x-ray absorption and infrared fuel cell spectroscopy", *Electrochim. Acta.* **56**, 8827 (2011).

Mark II operando fuel cell



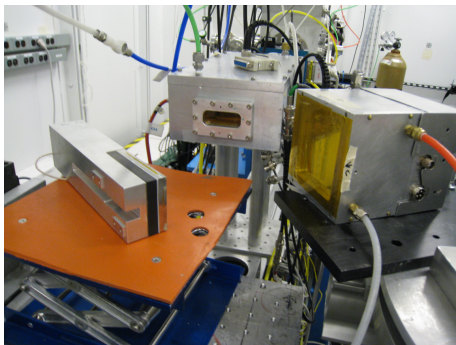
- Air-breathing cathode



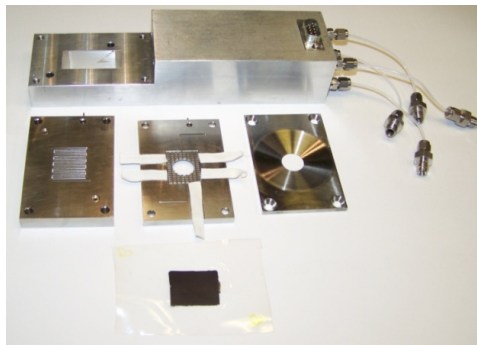
- Pd on anode

E.A. Lewis et al., "Operando x-ray absorption and infrared fuel cell spectroscopy", *Electrochim. Acta.* **56**, 8827 (2011).

Mark II operando fuel cell



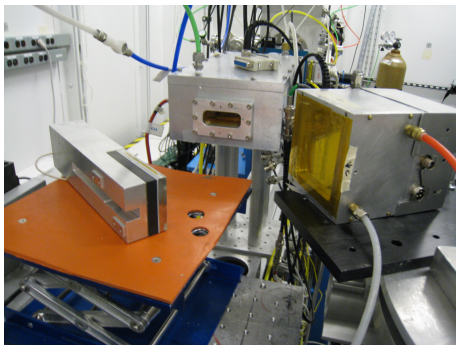
- Air-breathing cathode
- 1.2 mg/cm² loading



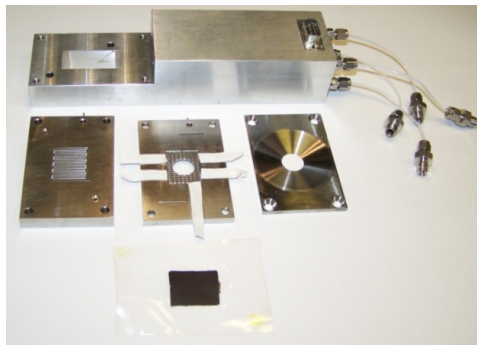
- Pd on anode

E.A. Lewis et al., "Operando x-ray absorption and infrared fuel cell spectroscopy", *Electrochim. Acta.* **56**, 8827 (2011).

Mark II operando fuel cell



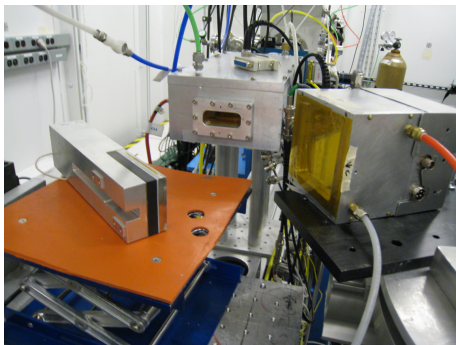
- Air-breathing cathode
- 1.2 mg/cm² loading



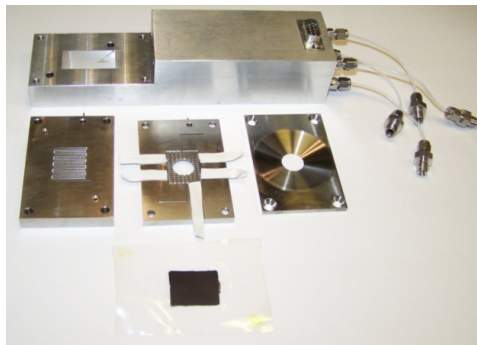
- Pd on anode
- 50°C operating temp

E.A. Lewis et al., "Operando x-ray absorption and infrared fuel cell spectroscopy", *Electrochim. Acta.* **56**, 8827 (2011).

Mark II operando fuel cell



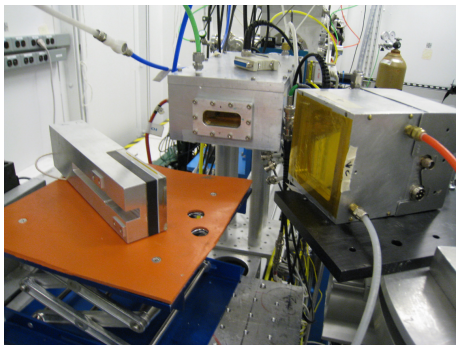
- Air-breathing cathode
- 1.2 mg/cm^2 loading
- Pt L₃ and Ni K edges



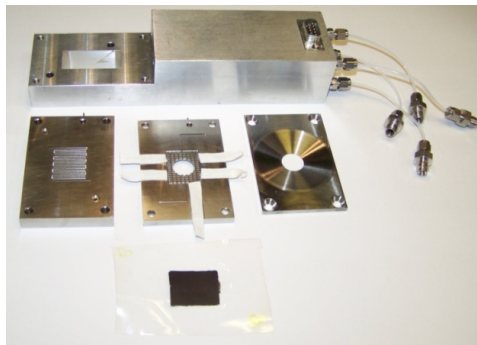
- Pd on anode
- 50°C operating temp

E.A. Lewis et al., "Operando x-ray absorption and infrared fuel cell spectroscopy", *Electrochim. Acta.* **56**, 8827 (2011).

Mark II operando fuel cell



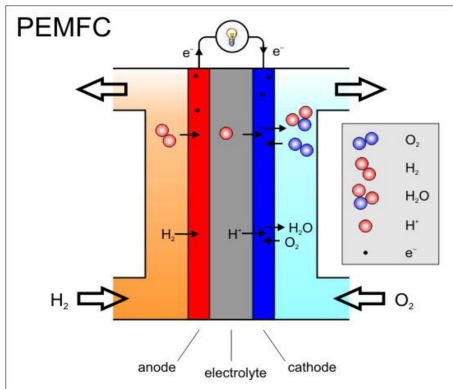
- Air-breathing cathode
- 1.2 mg/cm^2 loading
- Pt L₃ and Ni K edges



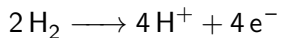
- Pd on anode
- 50°C operating temp
- Continuous scan mode

E.A. Lewis et al., "Operando x-ray absorption and infrared fuel cell spectroscopy", *Electrochim. Acta.* **56**, 8827 (2011).

Oxygen reduction at a PtNi cathode

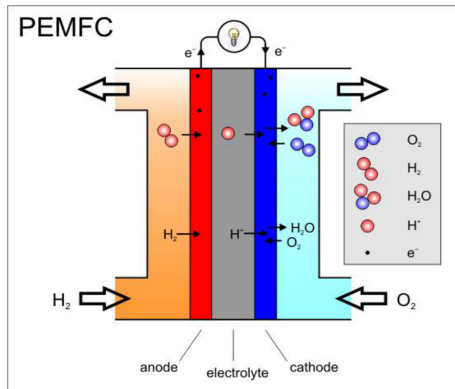


Anode: 0 V vs. SHE



U.S. Department of Defense (DoD) Fuel Cell Test and Evaluation Center (FCTec)

Oxygen reduction at a PtNi cathode



U.S. Department of Defense (DoD) Fuel Cell Test and Evaluation Center (FCTec)

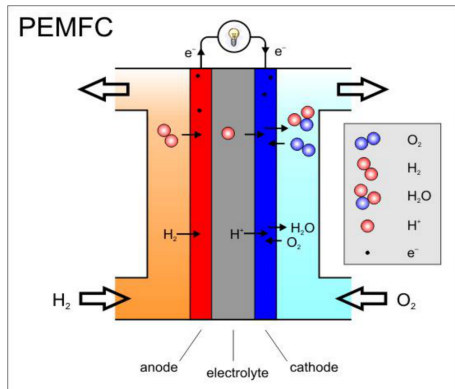
Anode: 0 V vs. SHE



Cathode: 1.23 V vs. SHE



Oxygen reduction at a PtNi cathode



U.S. Department of Defense (DoD) Fuel Cell Test and Evaluation Center (FCTec)

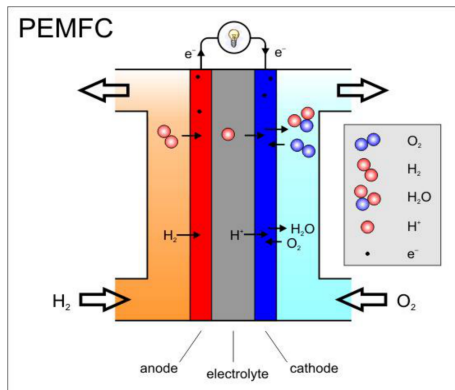
Anode: 0 V vs. SHE



Cathode: 1.23 V vs. SHE



Oxygen reduction at a PtNi cathode

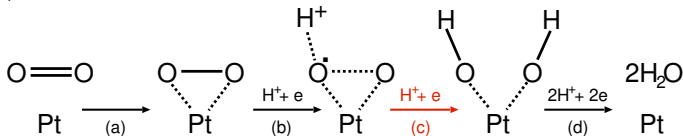
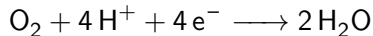


U.S. Department of Defense (DoD) Fuel Cell Test and Evaluation Center (FCTec)

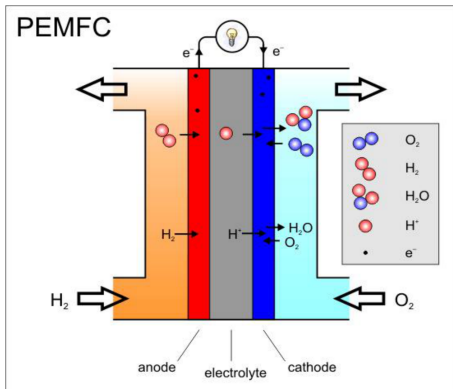
Anode: 0 V vs. SHE



Cathode: 1.23 V vs. SHE

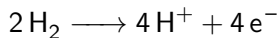


Oxygen reduction at a PtNi cathode



U.S. Department of Defense (DoD) Fuel Cell Test and Evaluation Center (FCTec)

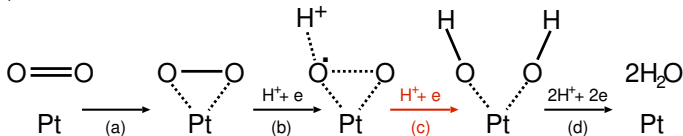
Anode: 0 V vs. SHE



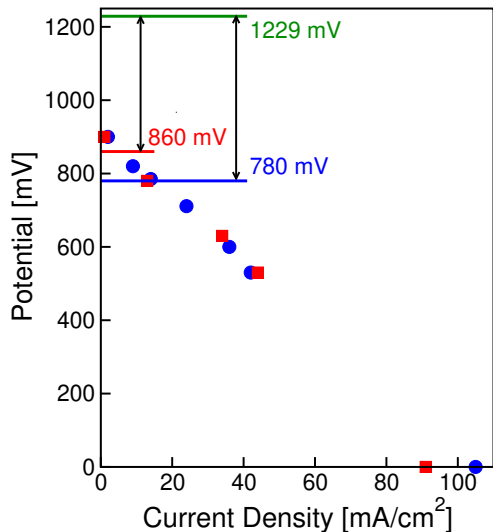
Cathode: 1.23 V vs. SHE



breaking O–O bond is the rate limiting step

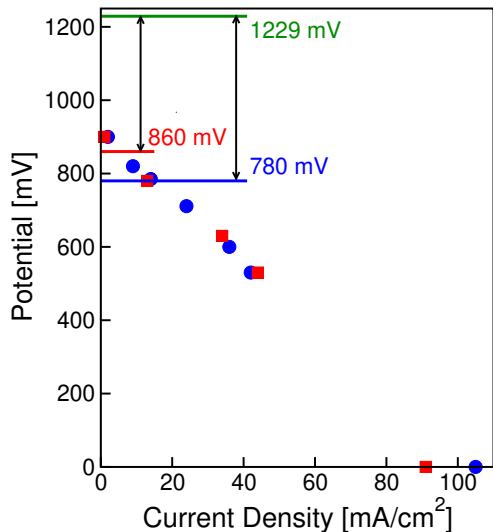


Fuel cell performance and open questions



PtNi/Pd has higher open circuit voltage, similar performance to Pt/Pd.

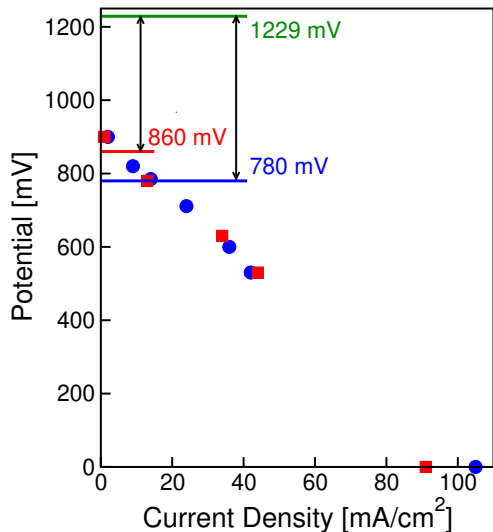
Fuel cell performance and open questions



PtNi/Pd has higher open circuit voltage, similar performance to Pt/Pd.

Why is ORR improved with bimetallic catalyst?

Fuel cell performance and open questions

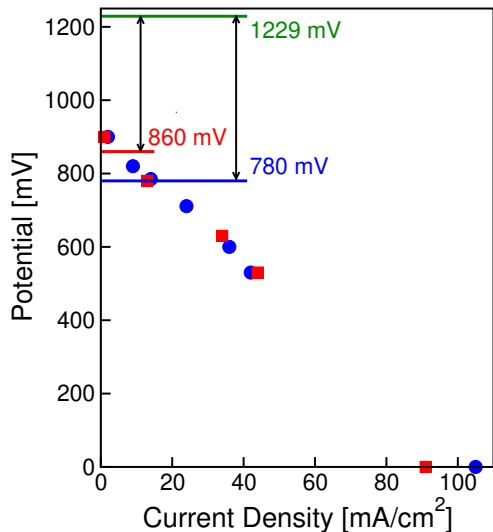


PtNi/Pd has higher open circuit voltage, similar performance to Pt/Pd.

Why is ORR improved with bimetallic catalyst?

- Pt electronic structure modified

Fuel cell performance and open questions

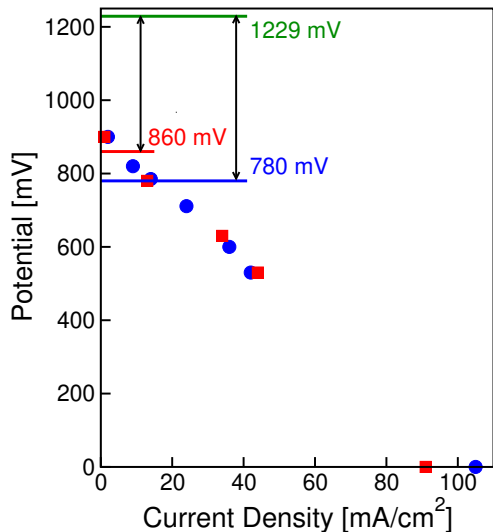


PtNi/Pd has higher open circuit voltage, similar performance to Pt/Pd.

Why is ORR improved with bimetallic catalyst?

- Pt electronic structure modified
- Pt catalyst geometric structure modified

Fuel cell performance and open questions

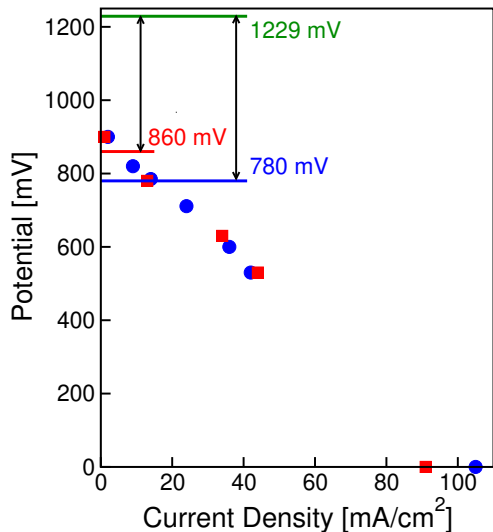


PtNi/Pd has higher open circuit voltage, similar performance to Pt/Pd.

Why is ORR improved with bimetallic catalyst?

- Pt electronic structure modified
- Pt catalyst geometric structure modified
- Static oxygen adsorbates inhibited

Fuel cell performance and open questions

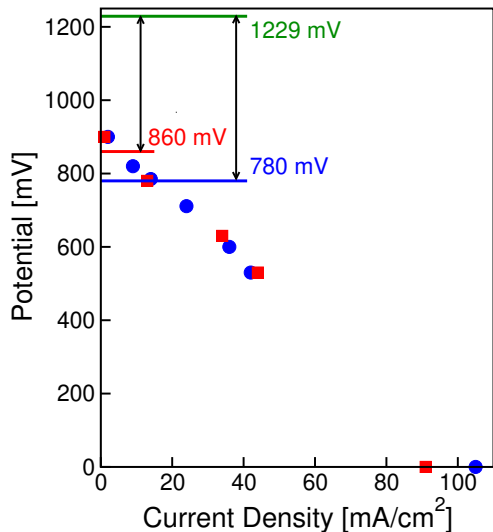


PtNi/Pd has higher open circuit voltage, similar performance to Pt/Pd.

Why is ORR improved with bimetallic catalyst?

- Pt electronic structure modified
- Pt catalyst geometric structure modified
- Static oxygen adsorbates inhibited
- Overpotential reduced

Fuel cell performance and open questions



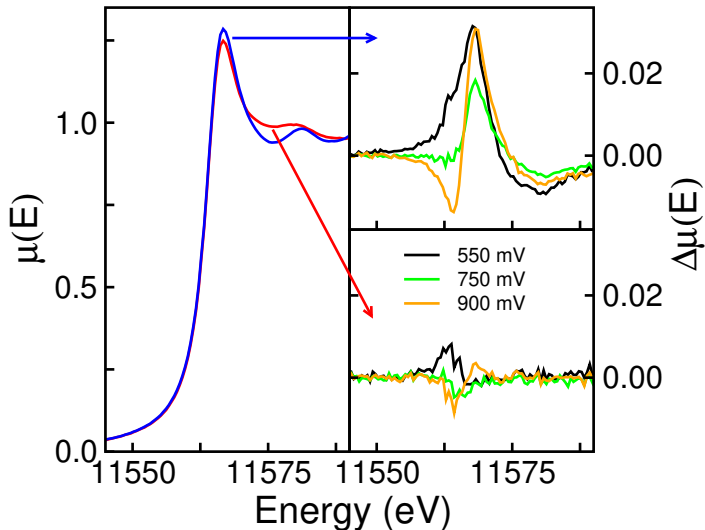
PtNi/Pd has higher open circuit voltage, similar performance to Pt/Pd.

Why is ORR improved with bimetallic catalyst?

- Pt electronic structure modified
- Pt catalyst geometric structure modified
- Static oxygen adsorbates inhibited
- Overpotential reduced

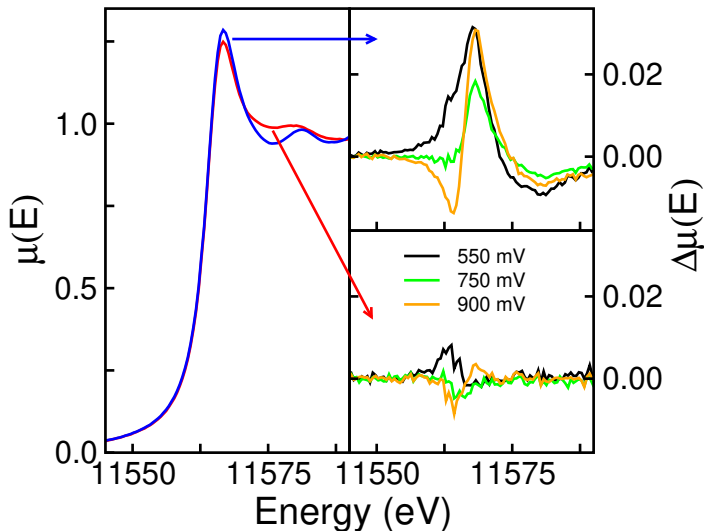
Using XAS to study the catalyst nanoparticles can help answer the first three questions

Pt/C and PtNi/C comparison



Q. Jia et al, "In Situ XAFS studies of the oxygen reduction reaction on carbon supported Pt and PtNi(1:1) catalysts", *J. Phys. Conf. Series* **190**, 012157 (2009).

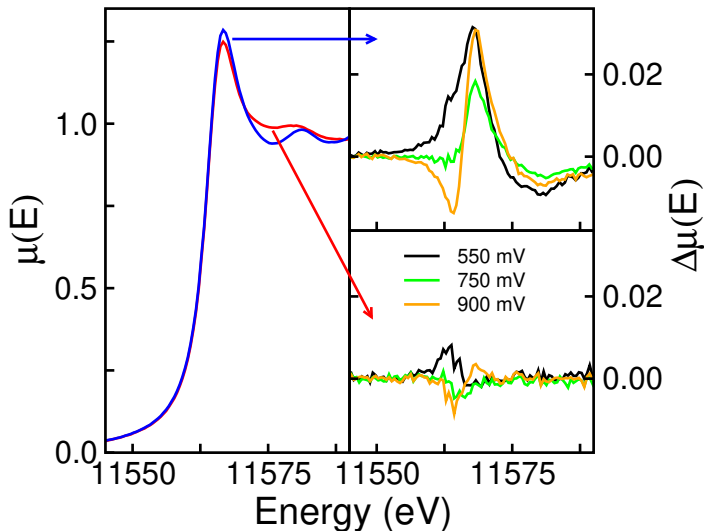
Pt/C and PtNi/C comparison



At highest potential, all catalysts are metallic and the Pt L₃ XANES shows significant difference between the Pt and PtNi catalysts

Q. Jia et al, "In Situ XAFS studies of the oxygen reduction reaction on carbon supported Pt and PtNi(1:1) catalysts", *J. Phys. Conf. Series* **190**, 012157 (2009).

Pt/C and PtNi/C comparison



At highest potential, all catalysts are metallic and the Pt L₃ XANES shows significant difference between the Pt and PtNi catalysts

Delta XANES shows a suppression of Pt oxidation in the PtNi catalyst as a function of applied potential

Q. Jia et al, "In Situ XAFS studies of the oxygen reduction reaction on carbon supported Pt and PtNi(1:1) catalysts", *J. Phys. Conf. Series* **190**, 012157 (2009).



Attempt to get global information about the oxygen



Attempt to get global information about the oxygen

Fit all potentials with same metal core parameters for each catalyst



Attempt to get global information about the oxygen

Fit all potentials with same metal core parameters for each catalyst

Simultaneous fit of Pt and Ni edges in PtNi/C with constraint on Pt-Ni distance



Attempt to get global information about the oxygen

Fit all potentials with same metal core parameters for each catalyst

Simultaneous fit of Pt and Ni edges in PtNi/C with constraint on Pt-Ni distance

Fit in k , k^2 , and k^3 weighting simultaneously



Attempt to get global information about the oxygen

Fit all potentials with same metal core parameters for each catalyst

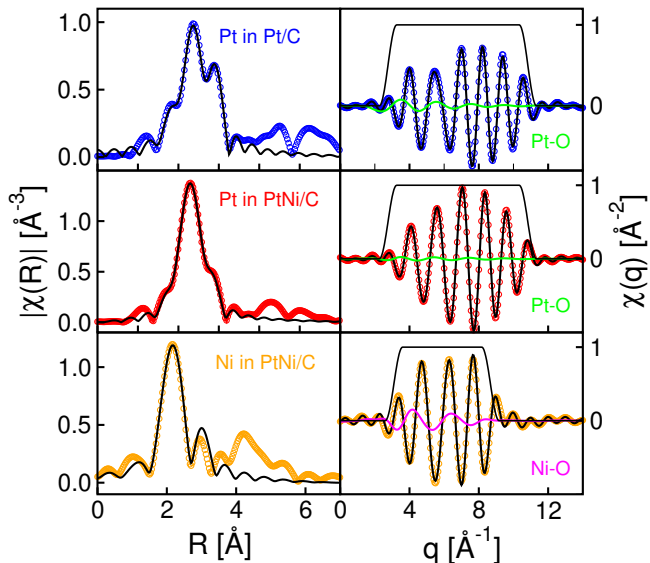
Simultaneous fit of Pt and Ni edges in PtNi/C with constraint on Pt-Ni distance

Fit in k , k^2 , and k^3 weighting simultaneously

Apply M-O path constraints

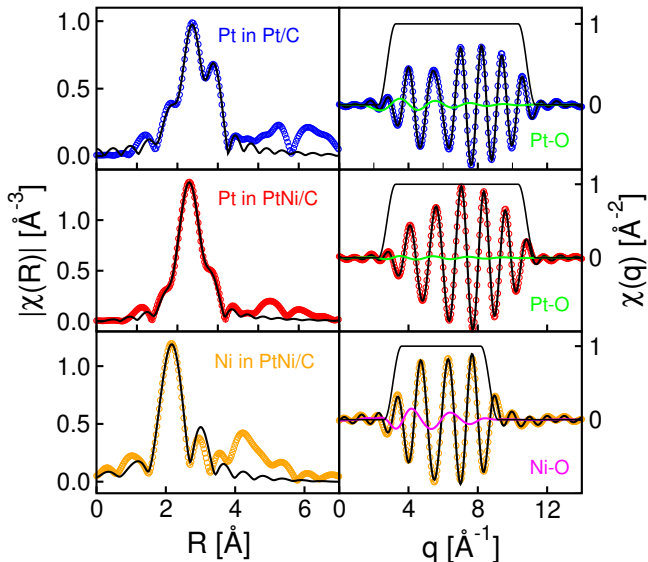
- length common across potentials
- σ^2 fixed to 0.01
- Pt-O in PtNi/C at all potentials are refined with a common occupation #

Example fits



"In Situ XAFS studies of the oxygen reduction reaction on carbon supported Pt and PtNi(1:1) catalysts", Q. Jia, E.A. Lewis, E.S. Smotkin, and C.U. Segre, *J. Phys. Conf. Series* **190**, 012157 (2009).

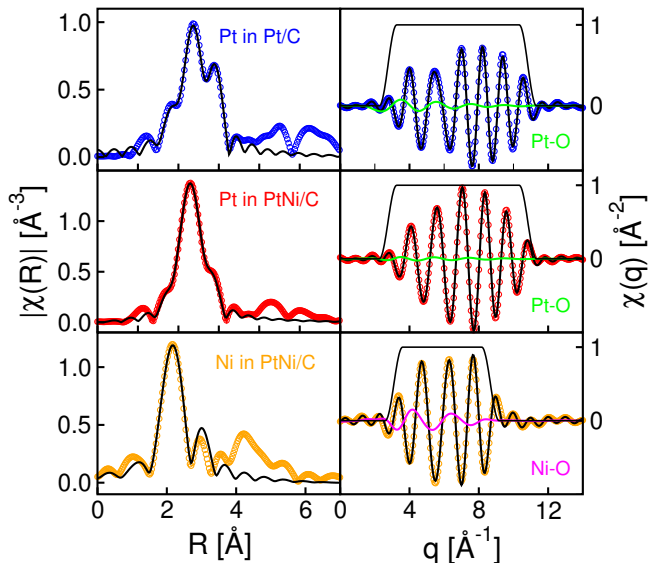
Example fits



Fits out to 3.5 Å in R-space and back
Fourier Transforms

"In Situ XAFS studies of the oxygen reduction reaction on carbon supported Pt and PtNi(1:1) catalysts", Q. Jia, E.A. Lewis, E.S. Smotkin, and C.U. Segre, *J. Phys. Conf. Series* **190**, 012157 (2009).

Example fits

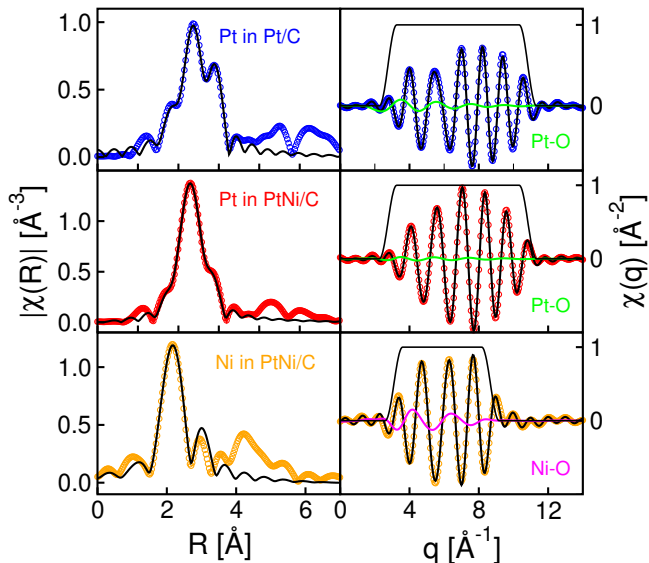


Fits out to 3.5 Å in R-space and back Fourier Transforms

The Pt catalyst shows a larger oxygen path contribution than the PtNi catalyst

"In Situ XAFS studies of the oxygen reduction reaction on carbon supported Pt and PtNi(1:1) catalysts", Q. Jia, E.A. Lewis, E.S. Smotkin, and C.U. Segre, *J. Phys. Conf. Series* **190**, 012157 (2009).

Example fits



Fits out to 3.5 \AA in R-space and back Fourier Transforms

The Pt catalyst shows a larger oxygen path contribution than the PtNi catalyst

The Ni EXAFS is dominated by the presence of a significant Ni-O bond

"In Situ XAFS studies of the oxygen reduction reaction on carbon supported Pt and PtNi(1:1) catalysts", Q. Jia, E.A. Lewis, E.S. Smotkin, and C.U. Segre, *J. Phys. Conf. Series* **190**, 012157 (2009).

Fit results



Pt/C	PtNi/C	
	Pt	Ni
N_{Pt} 8.7 ± 0.2	N_{Pt} 6.1 ± 0.3	N_{Ni} 3.7 ± 0.2
R_{Pt-Pt} 2.749 ± 0.001	R_{Pt-Pt} 2.692 ± 0.003	R_{Ni-Ni} 2.572 ± 0.006
	N_{Ni} 3.4 ± 0.1	N_{Pt} 8.9 ± 0.5
	R_{Pt-Ni} 2.635 ± 0.004	
	N_{Total} 9.5 ± 0.4	N_{Total} 12.6 ± 0.7
R_{Pt-O} 2.02 ± 0.01	R_{Pt-O} 2.09 ± 0.03	R_{Ni-O} 1.90 ± 0.01

Note the **Pt-Pt** and **Pt-O** bond lengths as well as **total metal near neighbors**

"In Situ XAFS studies of the oxygen reduction reaction on carbon supported Pt and PtNi(1:1) catalysts", Q. Jia, E.A. Lewis, E.S. Smotkin, and C.U. Segre, *J. Phys. Conf. Series* **190**, 012157 (2009).

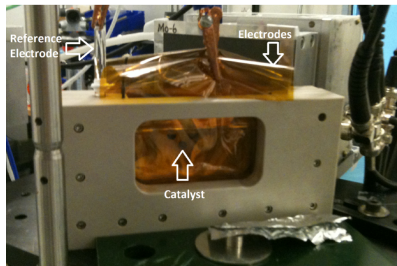
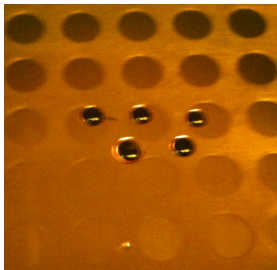
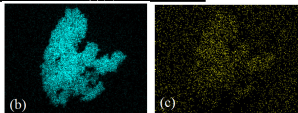
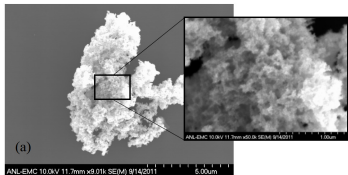
Role of Ru in CO oxidation?



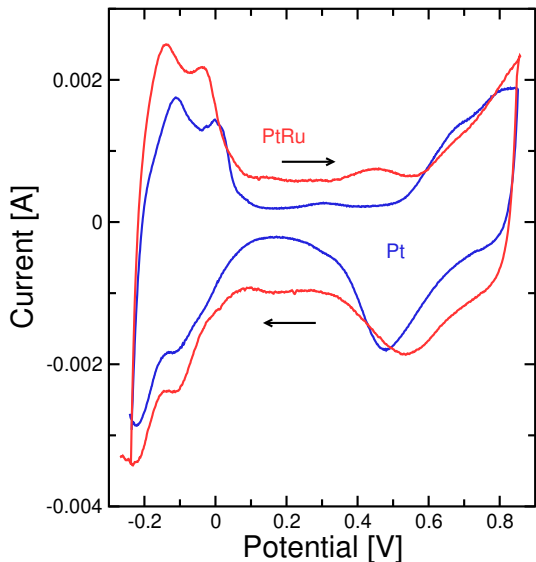
- PtRu bifunctional catalyst improves performance
- In commercial PtRu catalysts there is always a lot of inactive Ru-oxide (?)
- Ru signal dominated by metallic Ru environment
- How does Ru behave in the presence of reactants adsorbed on platinum surface?

Core-shell nanoparticles can resolve these questions

Ru-decorated Pt nanoparticles



Electrochemical performance



Without Methanol

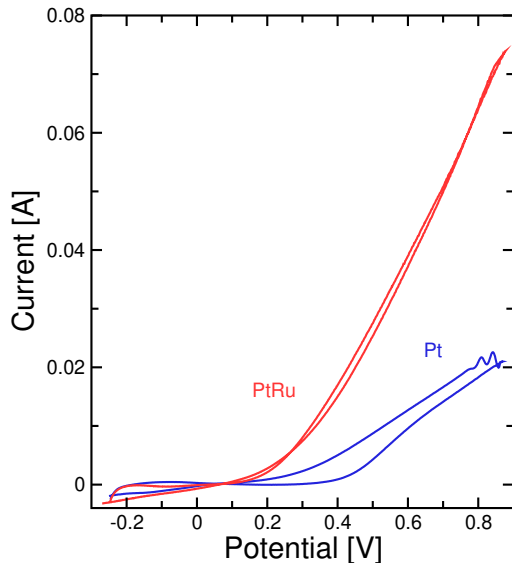
Low V peaks are H^+ stripping

Dip at ~ 0.5 V is oxygen stripping

Ru shifts potential on all peaks

"In situ Ru K-Edge x-ray absorption spectroscopy study of methanol oxidation mechanisms on model submonolayer Ru on Pt nanoparticle electrocatalyst," C.J. Pelliccione, E.V. Timofeeva, J.P. Katsoudas, and C.U. Segre, *J. Phys. Chem. C* **117**, 18904 (2013).

Electrochemical performance



Without Methanol

Low V peaks are H^+ stripping

Dip at ~ 0.5 V is oxygen stripping

Ru shifts potential on all peaks

With Methanol

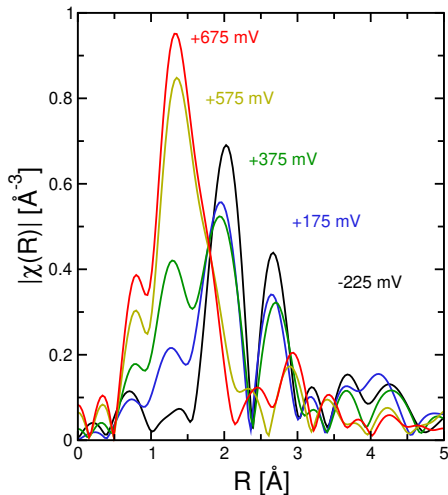
Continual current growth is due to methanol oxidation

Ru improves current by removing the CO which blocks active sites

"In situ Ru K-Edge x-ray absorption spectroscopy study of methanol oxidation mechanisms on model submonolayer Ru on Pt nanoparticle electrocatalyst," C.J. Pelllicione, E.V. Timofeeva, J.P. Katsoudas, and C.U. Segre, *J. Phys. Chem. C* **117**, 18904 (2013).

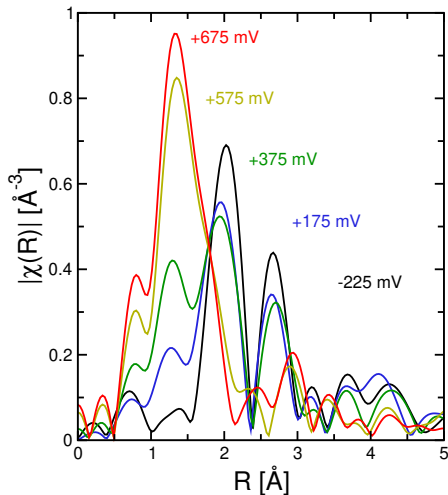


No methanol

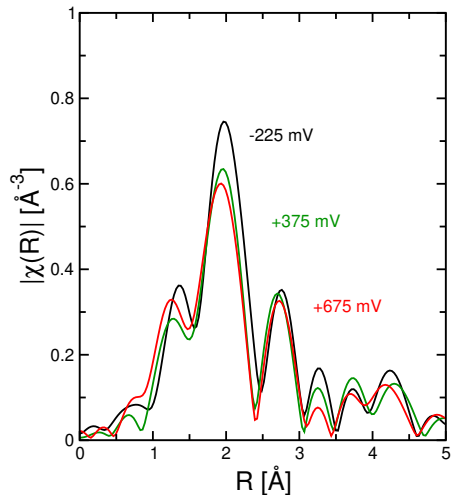


"In situ Ru K-Edge x-ray absorption spectroscopy study of methanol oxidation mechanisms on model submonolayer Ru on Pt nanoparticle electrocatalyst," C.J. Pelliccione, E.V. Timofeeva, J.P. Katsoudas, and C.U. Segre, *J. Phys. Chem. C* **117**, 18904 (2013).

No methanol

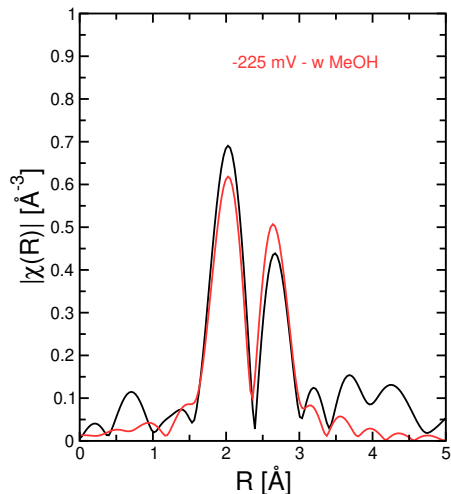
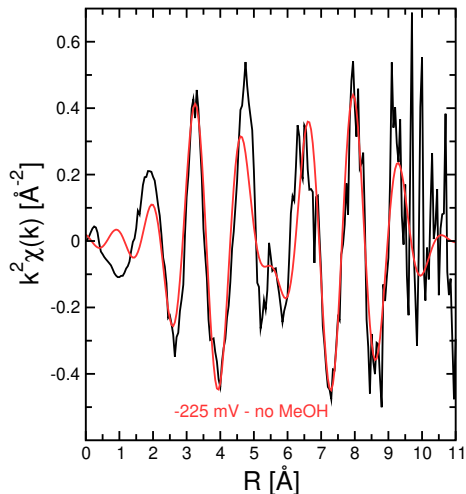


With methanol



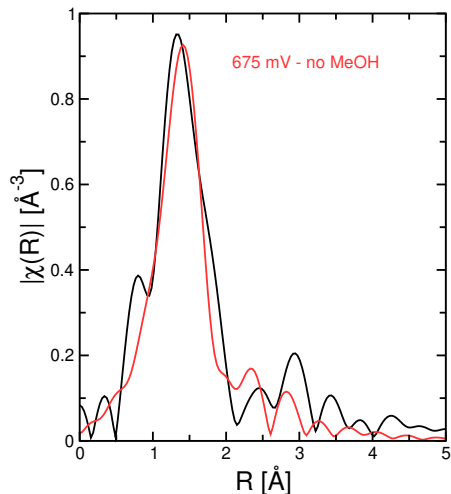
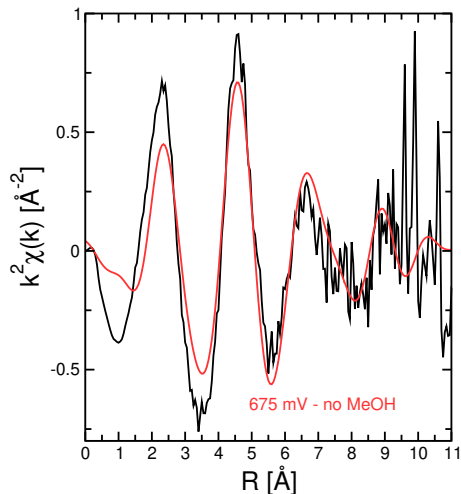
"In situ Ru K-Edge x-ray absorption spectroscopy study of methanol oxidation mechanisms on model submonolayer Ru on Pt nanoparticle electrocatalyst," C.J. Pelliccione, E.V. Timofeeva, J.P. Katsoudas, and C.U. Segre, *J. Phys. Chem. C* **117**, 18904 (2013).

Fit example: -225 mV without methanol



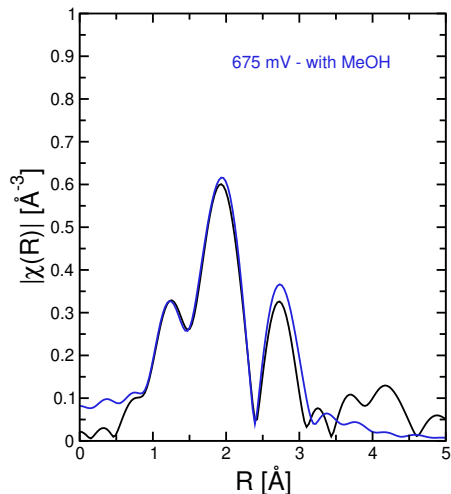
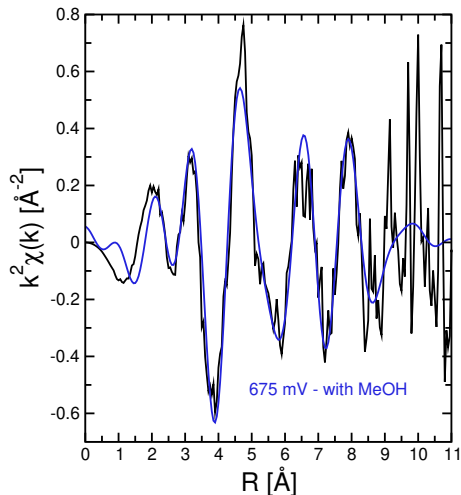
"In situ Ru K-Edge x-ray absorption spectroscopy study of methanol oxidation mechanisms on model submonolayer Ru on Pt nanoparticle electrocatalyst," C.J. Pelliccione, E.V. Timofeeva, J.P. Katsoudas, and C.U. Segre, *J. Phys. Chem. C* **117**, 18904 (2013).

Fit example: 675 mV without methanol

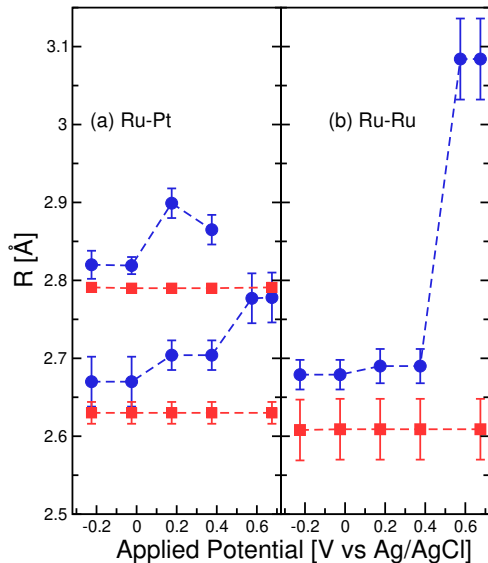


"In situ Ru K-Edge x-ray absorption spectroscopy study of methanol oxidation mechanisms on model submonolayer Ru on Pt nanoparticle electrocatalyst," C.J. Pelliccione, E.V. Timofeeva, J.P. Katsoudas, and C.U. Segre, *J. Phys. Chem. C* **117**, 18904 (2013).

Fit example: 675 mV with methanol



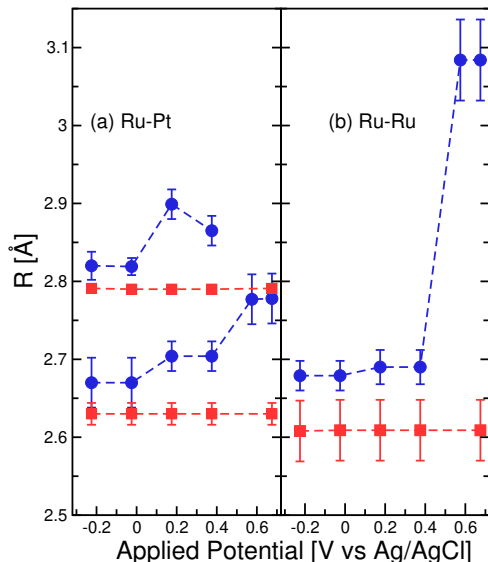
"In situ Ru K-Edge x-ray absorption spectroscopy study of methanol oxidation mechanisms on model submonolayer Ru on Pt nanoparticle electrocatalyst," C.J. Pelliccione, E.V. Timofeeva, J.P. Katsoudas, and C.U. Segre, *J. Phys. Chem. C* **117**, 18904 (2013).



Without methanol

With methanol

"In situ Ru K-Edge x-ray absorption spectroscopy study of methanol oxidation mechanisms on model submonolayer Ru on Pt nanoparticle electrocatalyst," C.J. Pelliccione, E.V. Timofeeva, J.P. Katsoudas, and C.U. Segre, *J. Phys. Chem. C* **117**, 18904 (2013).

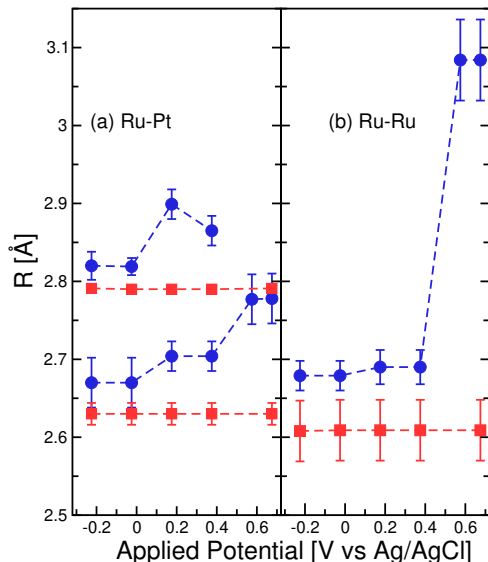


Without methanol

Ru-M distances are longer and RuO_2 is formed at high potentials

With methanol

"In situ Ru K-Edge x-ray absorption spectroscopy study of methanol oxidation mechanisms on model submonolayer Ru on Pt nanoparticle electrocatalyst," C.J. Pelliccione, E.V. Timofeeva, J.P. Katsoudas, and C.U. Segre, *J. Phys. Chem. C* **117**, 18904 (2013).



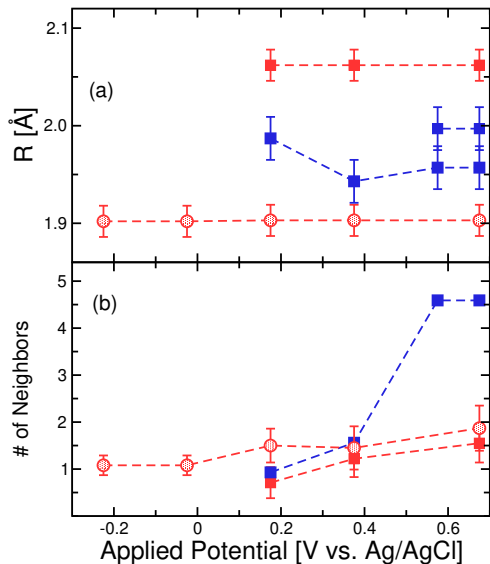
Without methanol

Ru-M distances are longer and RuO_2 is formed at high potentials

With methanol

Ru-M distances are shorter and remain the same at all potentials

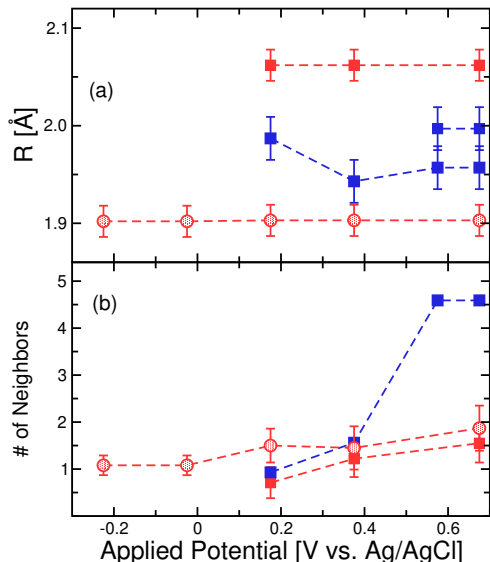
"In situ Ru K-Edge x-ray absorption spectroscopy study of methanol oxidation mechanisms on model submonolayer Ru on Pt nanoparticle electrocatalyst," C.J. Pelliccione, E.V. Timofeeva, J.P. Katsoudas, and C.U. Segre, *J. Phys. Chem. C* **117**, 18904 (2013).



Without methanol

With methanol

"In situ Ru K-Edge x-ray absorption spectroscopy study of methanol oxidation mechanisms on model submonolayer Ru on Pt nanoparticle electrocatalyst," C.J. Pelliccione, E.V. Timofeeva, J.P. Katsoudas, and C.U. Segre, *J. Phys. Chem. C* **117**, 18904 (2013).

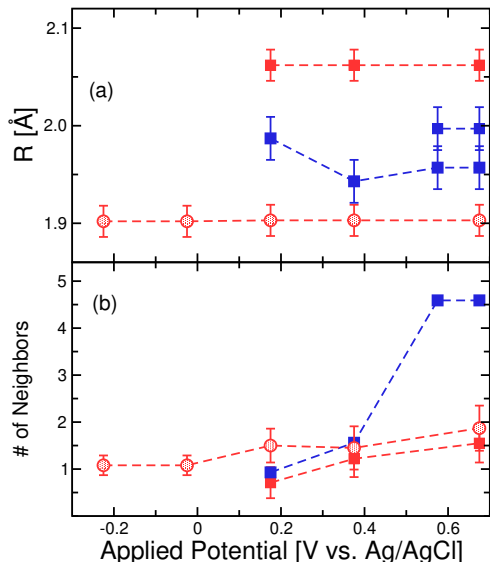


Without methanol

Above 375 mV Ru-O paths appear and total number of Ru-O neighbors increases to that of RuO₂

With methanol

"In situ Ru K-Edge x-ray absorption spectroscopy study of methanol oxidation mechanisms on model submonolayer Ru on Pt nanoparticle electrocatalyst," C.J. Pelliccione, E.V. Timofeeva, J.P. Katsoudas, and C.U. Segre, *J. Phys. Chem. C* **117**, 18904 (2013).



Without methanol

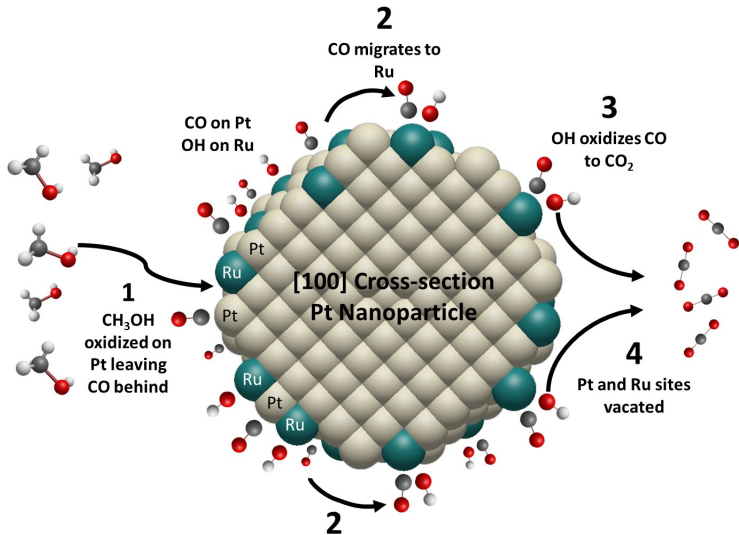
Above 375 mV Ru-O paths appear and total number of Ru-O neighbors increases to that of RuO₂

With methanol

Ru has one low Z neighbor at all potentials (carbon); a second above 175 mV (oxygen) with constant bond lengths and slightly increasing numbers

"In situ Ru K-Edge x-ray absorption spectroscopy study of methanol oxidation mechanisms on model submonolayer Ru on Pt nanoparticle electrocatalyst," C.J. Pelliccione, E.V. Timofeeva, J.P. Katsoudas, and C.U. Segre, *J. Phys. Chem. C* **117**, 18904 (2013).

Bi-functional mechanism

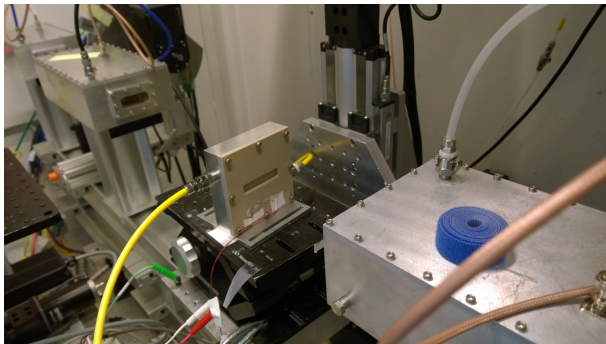


"In situ Ru K-Edge x-ray absorption spectroscopy study of methanol oxidation mechanisms on model submonolayer Ru on Pt nanoparticle electrocatalyst," C.J. Pelliccione, E.V. Timofeeva, J.P. Katsoudas, and C.U. Segre, *J. Phys. Chem. C* **117**, 18904 (2013).

In situ lithiation of Sn anode



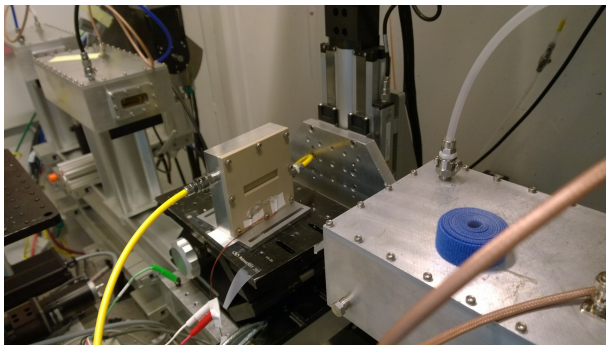
- In situ He-filled box for non-aqueous battery experiments



In situ lithiation of Sn anode



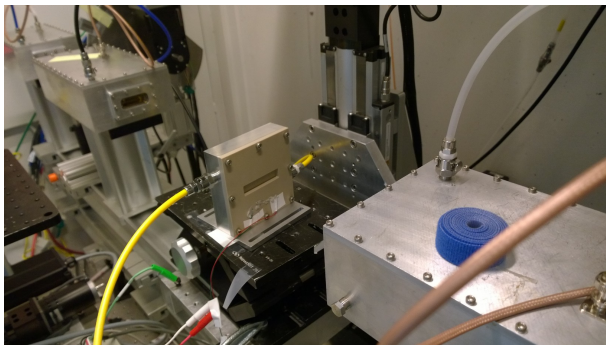
- In situ He-filled box for non-aqueous battery experiments
- Anode materials measured include: $\text{Sn}_3\text{O}_2(\text{OH})_2$, SnO_2 , Sn , ZnO , MoO_2 ...



In situ lithiation of Sn anode



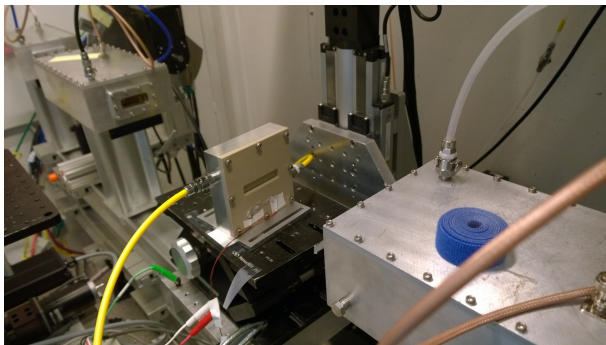
- In situ He-filled box for non-aqueous battery experiments
- Anode materials measured include: $\text{Sn}_3\text{O}_2(\text{OH})_2$, SnO_2 , **Sn**, ZnO , MoO_2 ...
- Pouch cell simplifies experiment



In situ lithiation of Sn anode



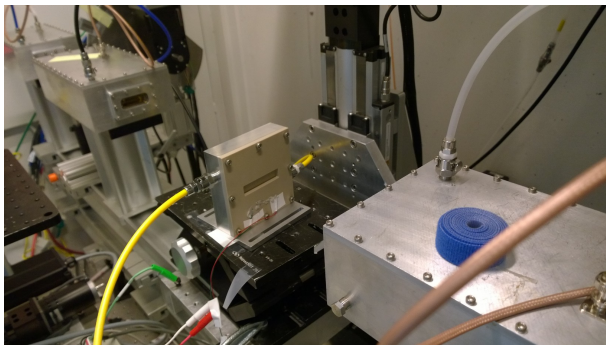
- In situ He-filled box for non-aqueous battery experiments
- Anode materials measured include: $\text{Sn}_3\text{O}_2(\text{OH})_2$, SnO_2 , Sn, ZnO , MoO_2 ...
- Pouch cell simplifies experiment
- MRCAT 10-ID beam line scans EXAFS spectrum in 2 minutes



In situ lithiation of Sn anode



- In situ He-filled box for non-aqueous battery experiments
- Anode materials measured include: $\text{Sn}_3\text{O}_2(\text{OH})_2$, SnO_2 , **Sn**, ZnO , MoO_2 ...
- Pouch cell simplifies experiment

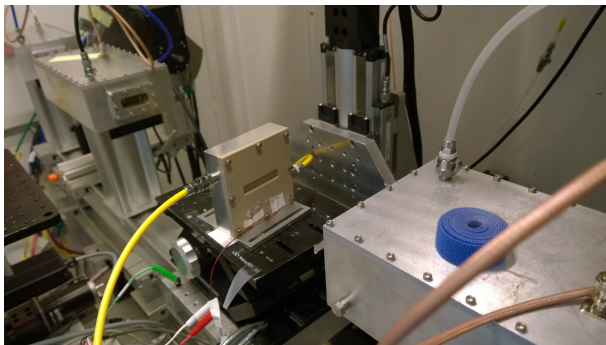


- MRCAT 10-ID beam line scans EXAFS spectrum in 2 minutes
- Focus on Sn nanoparticles which have rapid failure rate

In situ lithiation of Sn anode

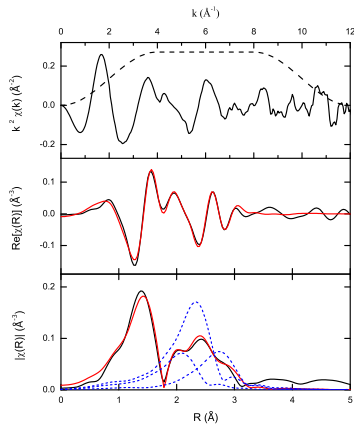


- In situ He-filled box for non-aqueous battery experiments
- Anode materials measured include: $\text{Sn}_3\text{O}_2(\text{OH})_2$, SnO_2 , Sn, ZnO, MoO_2 ...
- Pouch cell simplifies experiment



- MRCAT 10-ID beam line scans EXAFS spectrum in 2 minutes
- Focus on Sn nanoparticles which have rapid failure rate
- Develop modeled Sn-Li paths in $\text{Sn}_3\text{O}_2(\text{OH})_2$ using 3 composite paths

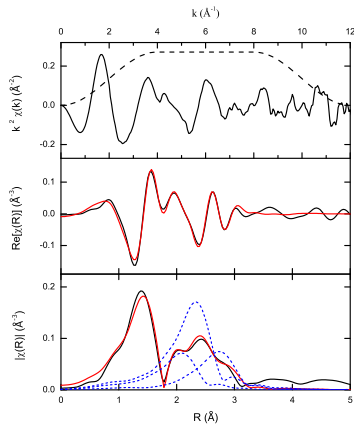
Initial *in situ* Sn-based anode EXAFS



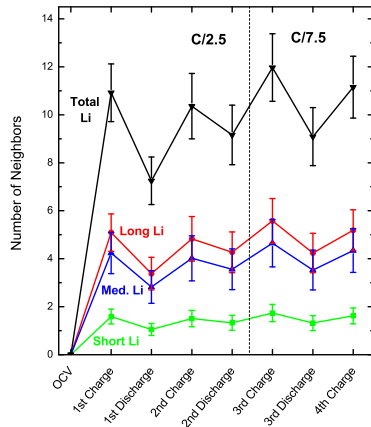
$\text{Li}_{22}\text{Sn}_5$ has 14 Sn-Li paths with distance of 3.4 \AA or less. Model with **three Sn-Li paths** at “center of mass” locations

“In situ XAS study of the capacity fading mechanism in hybrid $\text{Sn}_3\text{O}_2(\text{OH})_2$ /graphite battery anode nanomaterials,” C.J. Pelliccione, E.V. Timofeeva, and C.U. Segre, *Chem. Mater.* **27**, 574-580 (2015).

Initial *in situ* Sn-based anode EXAFS



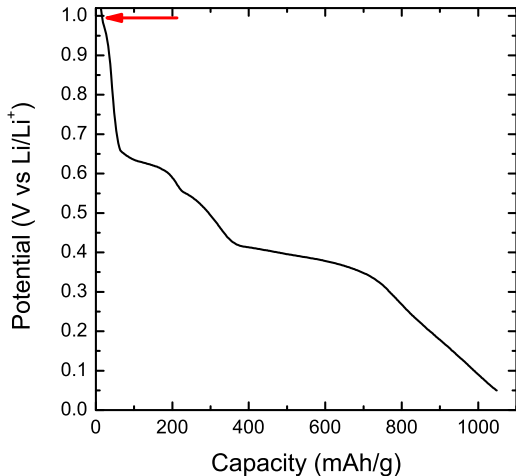
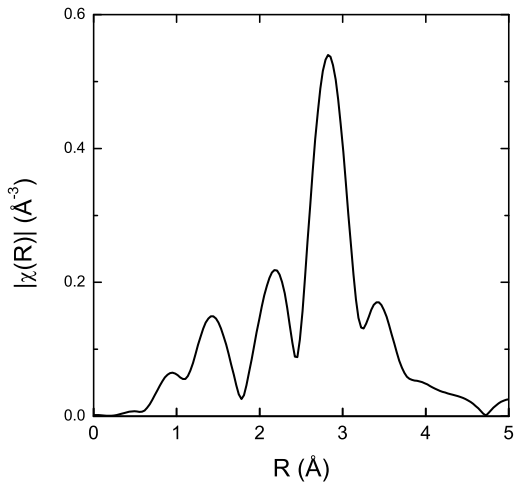
$\text{Li}_{22}\text{Sn}_5$ has 14 Sn-Li paths with distance of 3.4 Å or less. Model with three Sn-Li paths at “center of mass” locations



The number of Li near neighbors varies with lithiation and delithiation but shows how degradation progresses

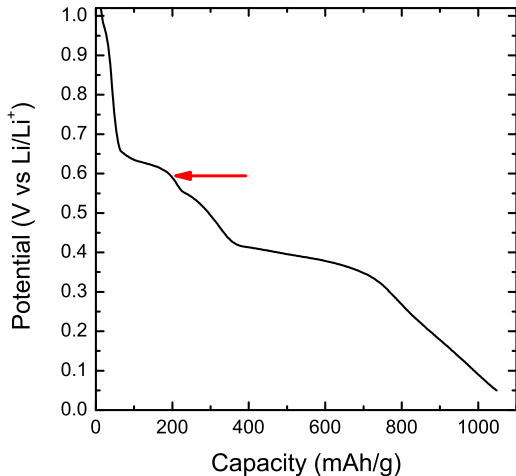
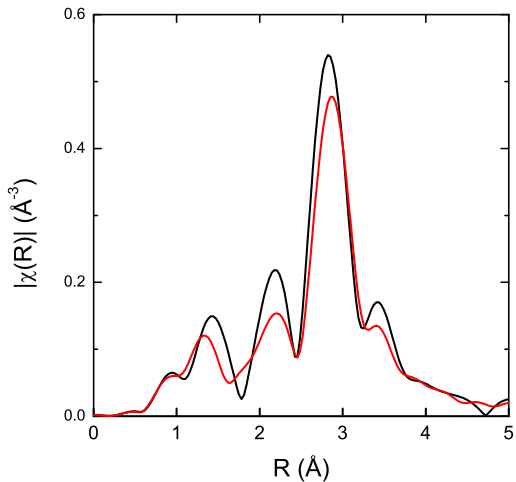
“In situ XAS study of the capacity fading mechanism in hybrid $\text{Sn}_3\text{O}_2(\text{OH})_2$ /graphite battery anode nanomaterials,” C.J. Pelliccione, E.V. Timofeeva, and C.U. Segre, *Chem. Mater.* **27**, 574-580 (2015).

Sn nanoparticles – EXAFS versus potential



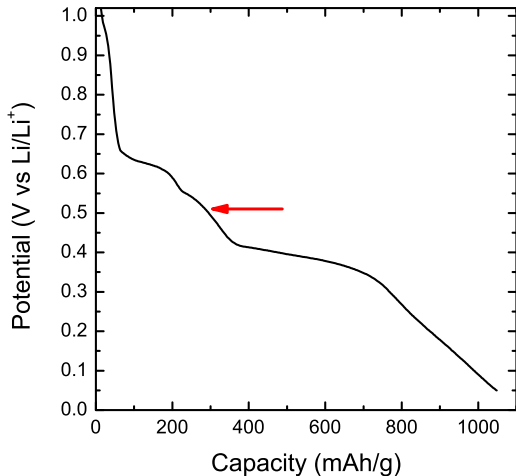
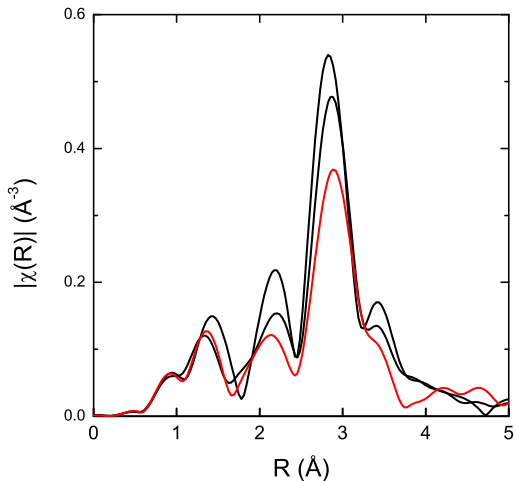
"Potential-resolved in situ x-ray absorption spectroscopy study of Sn and SnO_2 nanomaterial anodes for lithium-ion batteries," C.J. Pelliccione, E.V. Timofeeva, and C.U. Segre, *J. Phys. Chem. C* **120**, 5331-5339 (2016).

Sn nanoparticles – EXAFS versus potential



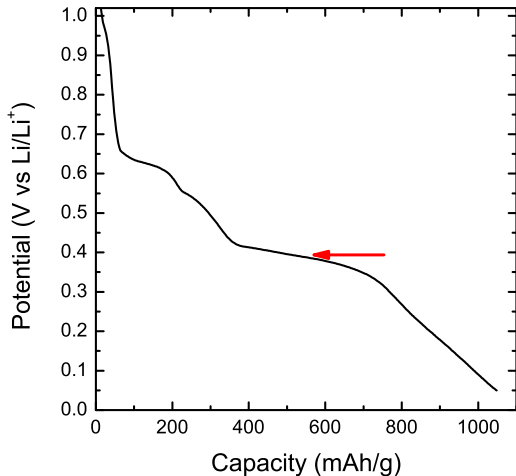
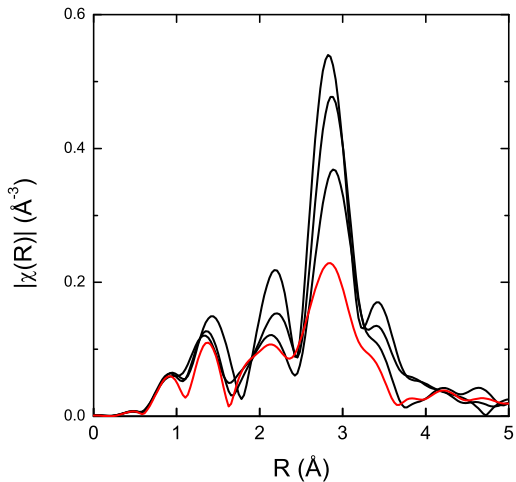
"Potential-resolved in situ x-ray absorption spectroscopy study of Sn and SnO_2 nanomaterial anodes for lithium-ion batteries," C.J. Pelliccione, E.V. Timofeeva, and C.U. Segre, *J. Phys. Chem. C* **120**, 5331-5339 (2016).

Sn nanoparticles – EXAFS versus potential



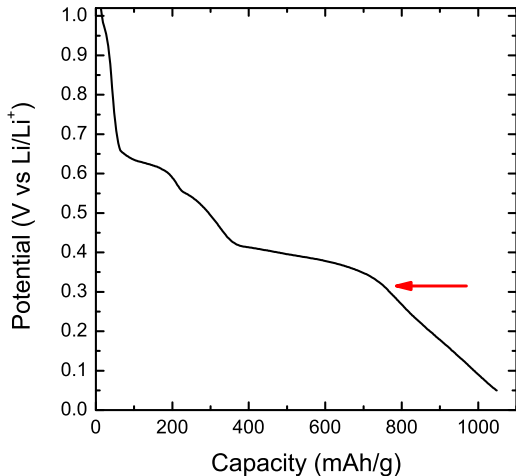
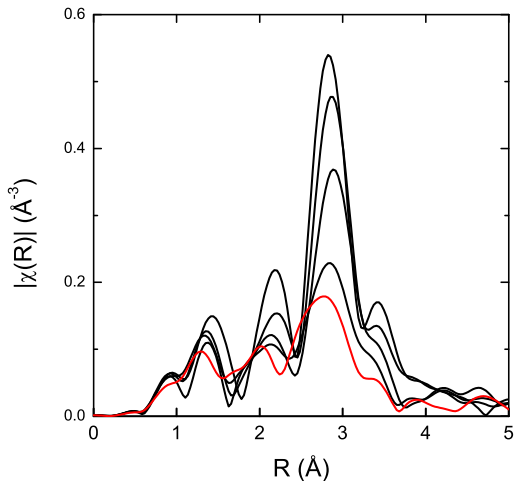
"Potential-resolved in situ x-ray absorption spectroscopy study of Sn and SnO_2 nanomaterial anodes for lithium-ion batteries," C.J. Pelliccione, E.V. Timofeeva, and C.U. Segre, *J. Phys. Chem. C* **120**, 5331-5339 (2016).

Sn nanoparticles – EXAFS versus potential



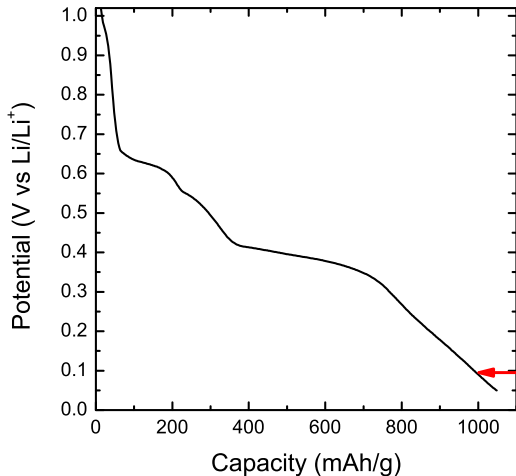
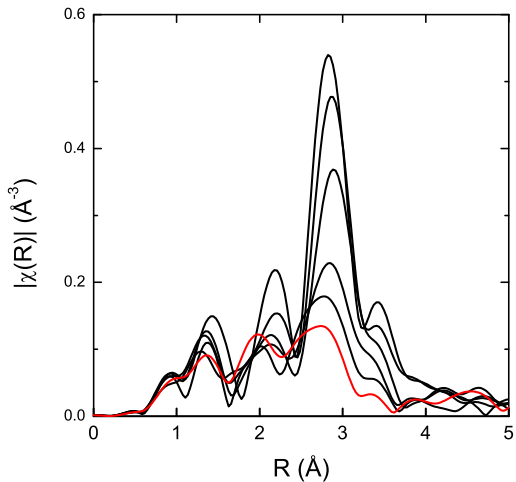
"Potential-resolved in situ x-ray absorption spectroscopy study of Sn and SnO_2 nanomaterial anodes for lithium-ion batteries," C.J. Pelliccione, E.V. Timofeeva, and C.U. Segre, *J. Phys. Chem. C* **120**, 5331-5339 (2016).

Sn nanoparticles – EXAFS versus potential



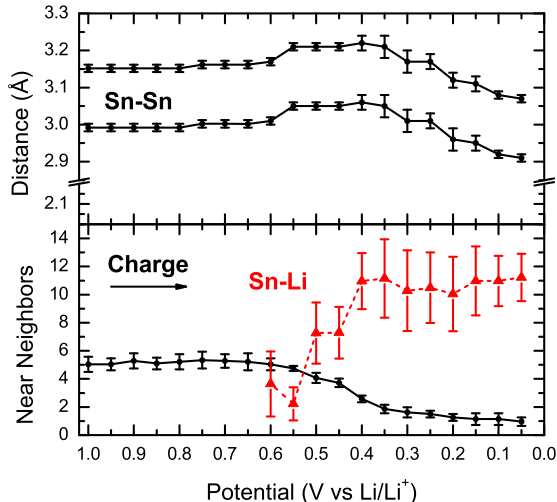
"Potential-resolved in situ x-ray absorption spectroscopy study of Sn and SnO_2 nanomaterial anodes for lithium-ion batteries," C.J. Pelliccione, E.V. Timofeeva, and C.U. Segre, *J. Phys. Chem. C* **120**, 5331-5339 (2016).

Sn nanoparticles – EXAFS versus potential



"Potential-resolved in situ x-ray absorption spectroscopy study of Sn and SnO_2 nanomaterial anodes for lithium-ion batteries," C.J. Pelliccione, E.V. Timofeeva, and C.U. Segre, *J. Phys. Chem. C* **120**, 5331-5339 (2016).

The Sn lithiation process



0.60V – Sn metal begins to break down and Li appears

0.45V – number of Li reaches 11 and stabilizes at near full Li₂₂Sn₅

However, Sn fades rapidly due to electric conductivity loss. What can be improved?

"Potential-resolved in situ x-ray absorption spectroscopy study of Sn and SnO₂ nanomaterial anodes for lithium-ion batteries," C.J. Pelliccione, E.V. Timofeeva, and C.U. Segre, *J. Phys. Chem. C* **120**, 5331-5339 (2016).



Sn₄P₃/graphite composite anode

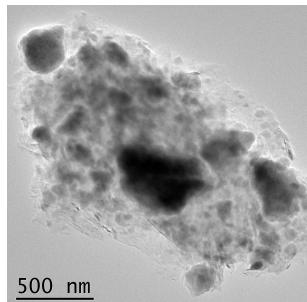
Sn₄P₃ synthesized by high energy ball milling, then ball milled again with graphite to obtain composite

"In situ EXAFS-derived mechanism of highly reversible tin phosphide/graphite composite anode for Li-ion batteries," Y. Ding, Z. Li, E.V. Timofeeva, and C.U. Segre, *Adv. Energy Mater.* **8**, 1702134 (2018).



Sn_4P_3 /graphite composite anode

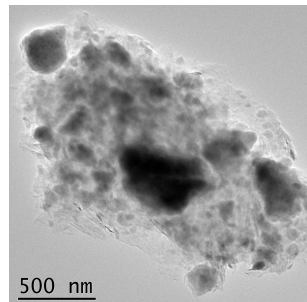
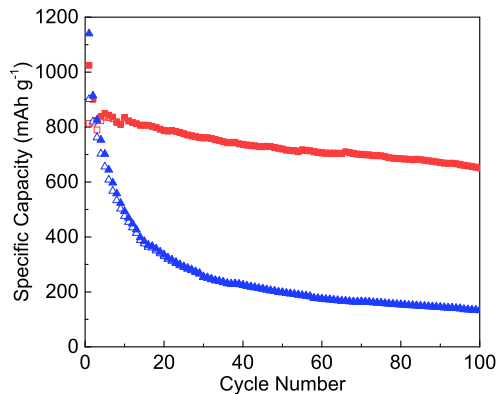
Sn_4P_3 synthesized by high energy ball milling, then ball milled again with graphite to obtain composite



"In situ EXAFS-derived mechanism of highly reversible tin phosphide/graphite composite anode for Li-ion batteries," Y. Ding, Z. Li, E.V. Timofeeva, and C.U. Segre, *Adv. Energy Mater.* **8**, 1702134 (2018).

Sn_4P_3 /graphite composite anode

Sn_4P_3 synthesized by high energy ball milling, then ball milled again with graphite to obtain composite

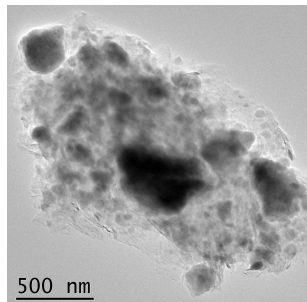
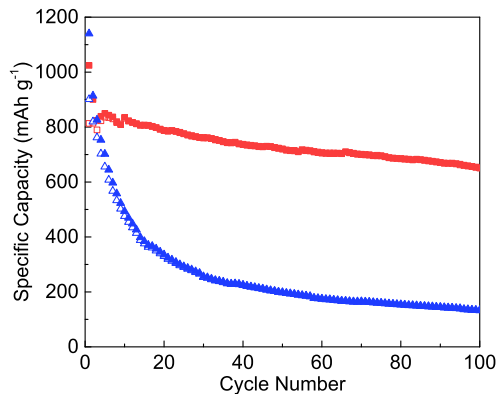


"In situ EXAFS-derived mechanism of highly reversible tin phosphide/graphite composite anode for Li-ion batteries," Y. Ding, Z. Li, E.V. Timofeeva, and C.U. Segre, *Adv. Energy Mater.* **8**, 1702134 (2018).



Sn_4P_3 /graphite composite anode

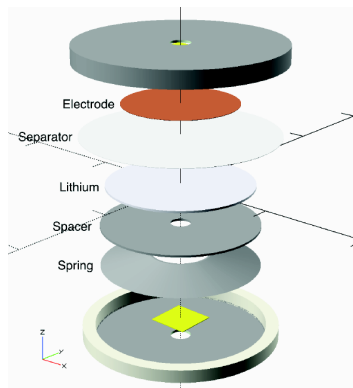
Sn_4P_3 synthesized by high energy ball milling, then ball milled again with graphite to obtain composite



Sn_4P_3 /graphite composite shows stable, reversible capacity of 610 mAh/g for 100 cycles at C/2 compared to rapidly fading pure Sn_4P_3 material.

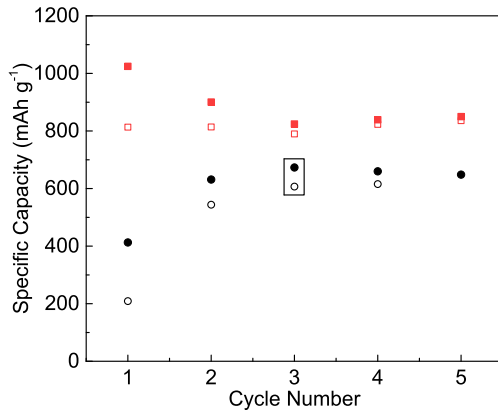
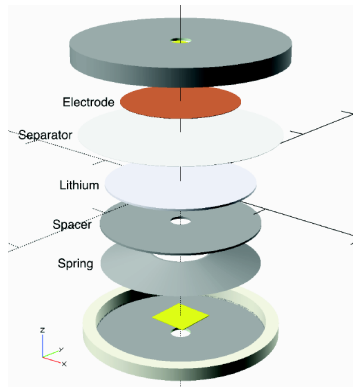
"In situ EXAFS-derived mechanism of highly reversible tin phosphide/graphite composite anode for Li-ion batteries," Y. Ding, Z. Li, E.V. Timofeeva, and C.U. Segre, *Adv. Energy Mater.* **8**, 1702134 (2018).

In situ EXAFS of Sn₄P₃/graphite



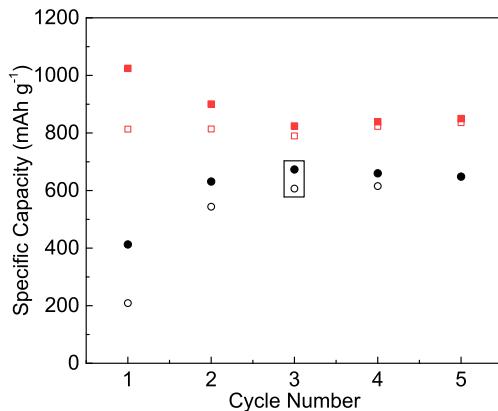
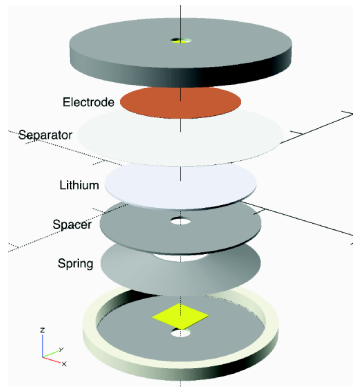
"In situ EXAFS-derived mechanism of highly reversible tin phosphide/graphite composite anode for Li-ion batteries," Y. Ding, Z. Li, E.V. Timofeeva, and C.U. Segre, *Adv. Energy Mater.* **8**, 1702134 (2018).

In situ EXAFS of Sn₄P₃/graphite



"In situ EXAFS-derived mechanism of highly reversible tin phosphide/graphite composite anode for Li-ion batteries," Y. Ding, Z. Li, E.V. Timofeeva, and C.U. Segre, *Adv. Energy Mater.* **8**, 1702134 (2018).

In situ EXAFS of Sn₄P₃/graphite



Results for *in situ* coin cell are close to the capacity of the unmodified cell at C/4, indicating good reversibility by the 3rd cycle.

"In situ EXAFS-derived mechanism of highly reversible tin phosphide/graphite composite anode for Li-ion batteries," Y. Ding, Z. Li, E.V. Timofeeva, and C.U. Segre, *Adv. Energy Mater.* **8**, 1702134 (2018).

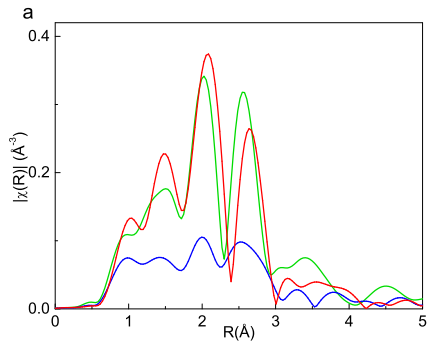
Third cycle comparison



By the third lithiation and third delithiation, the difference between pure Sn_4P_3 and the $\text{Sn}_4\text{P}_3/\text{graphite}$ composite is clear.

"In situ EXAFS-derived mechanism of highly reversible tin phosphide/graphite composite anode for Li-ion batteries," Y. Ding, Z. Li, E.V. Timofeeva, and C.U. Segre, *Adv. Energy Mater.* **8**, 1702134 (2018).

Third cycle comparison

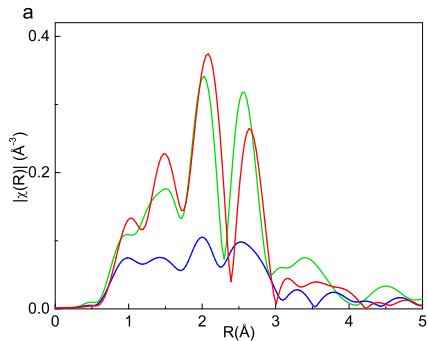


$\text{Sn}_4\text{P}_3/\text{graphite}$ composite

By the third lithiation and third delithiation, the difference between pure Sn_4P_3 and the $\text{Sn}_4\text{P}_3/\text{graphite}$ composite is clear.

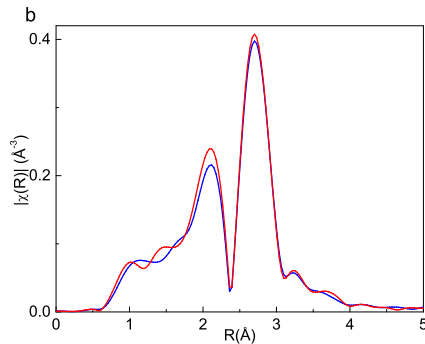
"In situ EXAFS-derived mechanism of highly reversible tin phosphide/graphite composite anode for Li-ion batteries," Y. Ding, Z. Li, E.V. Timofeeva, and C.U. Segre, *Adv. Energy Mater.* **8**, 1702134 (2018).

Third cycle comparison



Sn₄P₃/graphite composite

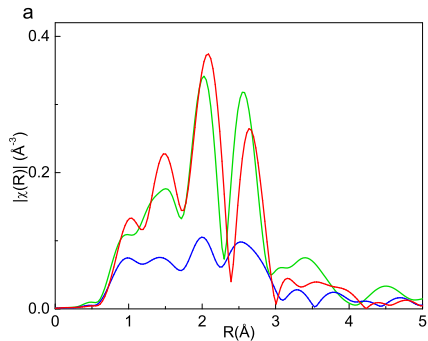
By the third lithiation and third delithiation, the difference between pure Sn₄P₃ and the Sn₄P₃/graphite composite is clear.



pure Sn₄P₃

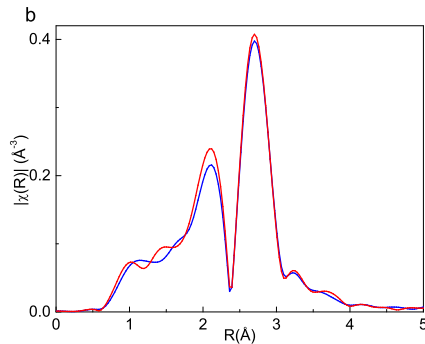
"In situ EXAFS-derived mechanism of highly reversible tin phosphide/graphite composite anode for Li-ion batteries," Y. Ding, Z. Li, E.V. Timofeeva, and C.U. Segre, *Adv. Energy Mater.* **8**, 1702134 (2018).

Third cycle comparison



Sn₄P₃/graphite composite

By the **third lithiation** and **third delithiation**, the difference between pure Sn₄P₃ and the Sn₄P₃/graphite composite is clear.



pure Sn₄P₃

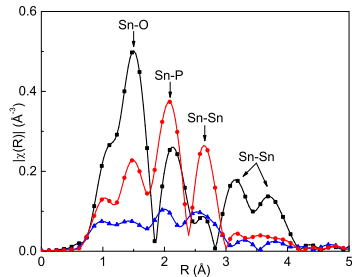
Even at the **100th delithiation**, the Sn₄P₃/graphite composite measured *ex situ* is showing the same features as at the **3rd** cycle.

"In situ EXAFS-derived mechanism of highly reversible tin phosphide/graphite composite anode for Li-ion batteries," Y. Ding, Z. Li, E.V. Timofeeva, and C.U. Segre, *Adv. Energy Mater.* **8**, 1702134 (2018).

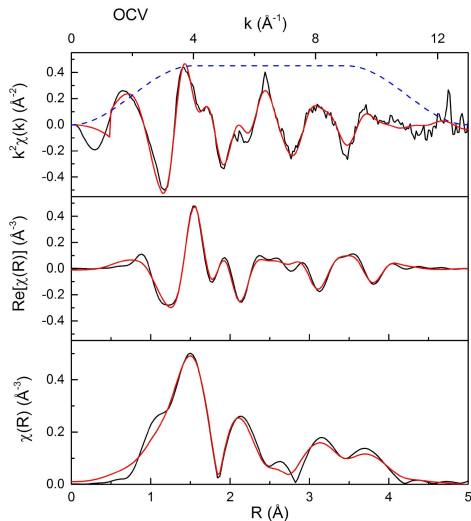
Example fits



Fit EXAFS for bond lengths and coordination numbers



The Sn-O peak at OCV is due to ball milling, which introduces oxygen.

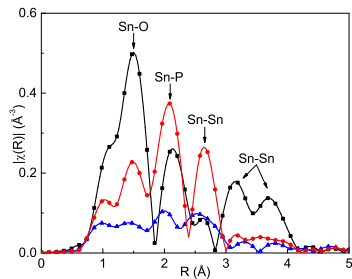


"In situ EXAFS-derived mechanism of highly reversible tin phosphide/graphite composite anode for Li-ion batteries," Y. Ding, Z. Li, E.V. Timofeeva, and C.U. Segre, *Adv. Energy Mater.* **8**, 1702134 (2018).

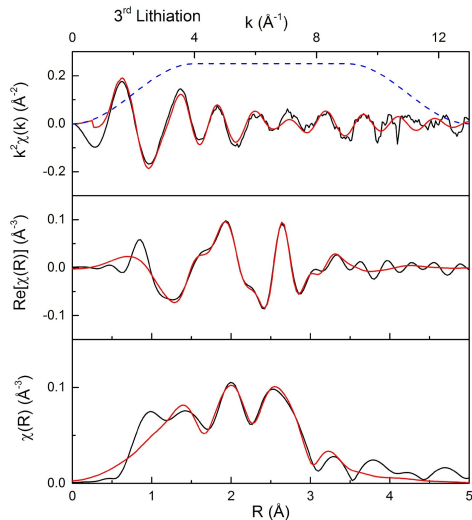
Example fits



Fit EXAFS for bond lengths and coordination numbers



By the 3rd lithiated state, the EXAFS is dominated by Sn-Li paths at 2.7 \AA and 3.0 \AA .

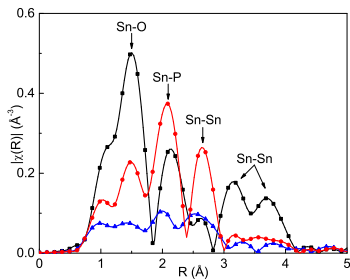


"In situ EXAFS-derived mechanism of highly reversible tin phosphide/graphite composite anode for Li-ion batteries," Y. Ding, Z. Li, E.V. Timofeeva, and C.U. Segre, *Adv. Energy Mater.* **8**, 1702134 (2018).

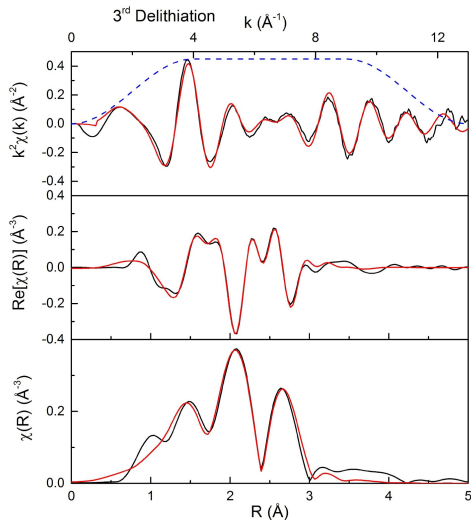


Example fits

Fit EXAFS for bond lengths and coordination numbers

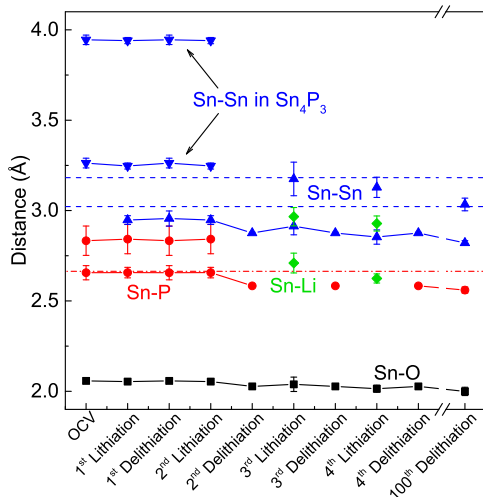


At the **3rd delithiation**, the Sn-P path reappears but at a shorter distance, in an amorphous SnP_x phase.



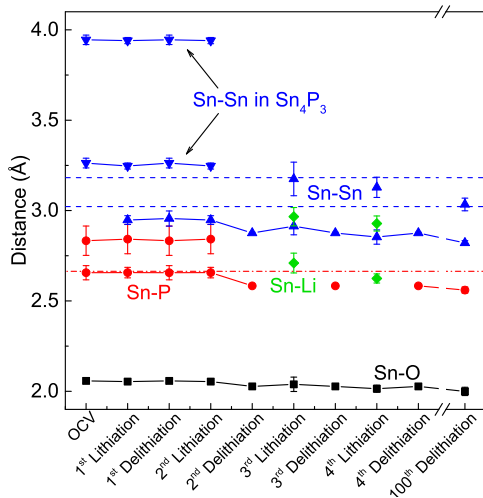
"In situ EXAFS-derived mechanism of highly reversible tin phosphide/graphite composite anode for Li-ion batteries," Y. Ding, Z. Li, E.V. Timofeeva, and C.U. Segre, *Adv. Energy Mater.* **8**, 1702134 (2018).

Sn₄P₃/graphite path lengths



Y. Ding et al., "In situ EXAFS-derived mechanism of highly reversible tin phosphide/graphite composite anode for Li-ion batteries," Y. Ding, Z. Li, E.V. Timofeeva, and C.U. Segre, *Adv. Energy Mater.* **8**, 1702134 (2018).

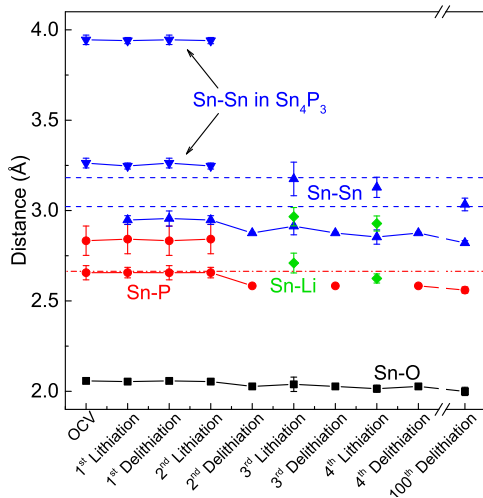
Sn₄P₃/graphite path lengths



Sn-Sn distance close to those of metallic Sn indicate the presence of small Sn clusters which may never fully lithiate

Y. Ding et al., "In situ EXAFS-derived mechanism of highly reversible tin phosphide/graphite composite anode for Li-ion batteries," Y. Ding, Z. Li, E.V. Timofeeva, and C.U. Segre, *Adv. Energy Mater.* **8**, 1702134 (2018).

Sn₄P₃/graphite path lengths

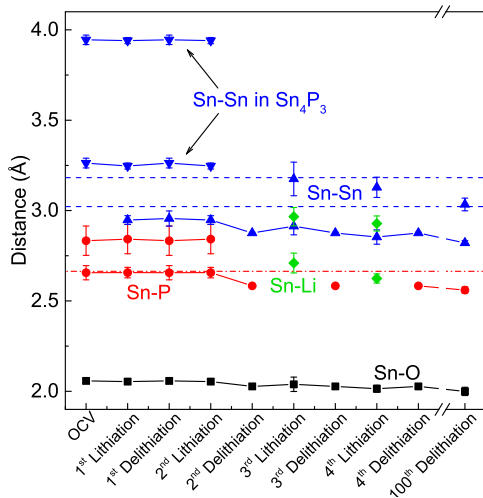


Sn-Sn distance close to those of metallic Sn indicate the presence of small Sn clusters which may never fully lithiate

Longer Sn-P distance characteristic of Sn₄P₃ is gone after initial conversion to the SnP_x amorphous phase is complete

Y. Ding et al., "In situ EXAFS-derived mechanism of highly reversible tin phosphide/graphite composite anode for Li-ion batteries," Y. Ding, Z. Li, E.V. Timofeeva, and C.U. Segre, *Adv. Energy Mater.* **8**, 1702134 (2018).

Sn₄P₃/graphite path lengths



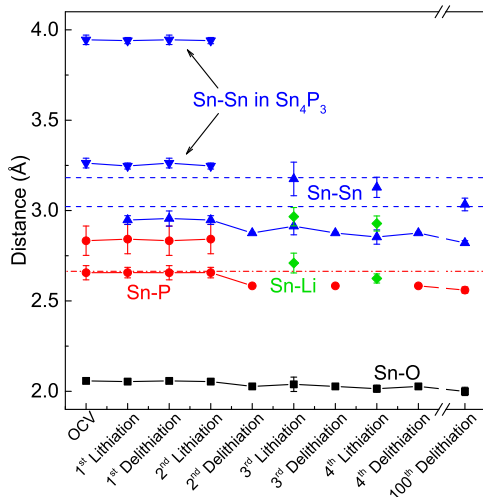
Sn-Sn distance close to those of metallic Sn indicate the presence of small Sn clusters which may never fully lithiate

Longer Sn-P distance characteristic of Sn₄P₃ is gone after initial conversion to the SnP_x amorphous phase is complete

Only 2 Sn-Li paths present in this material

Y. Ding et al., "In situ EXAFS-derived mechanism of highly reversible tin phosphide/graphite composite anode for Li-ion batteries," Y. Ding, Z. Li, E.V. Timofeeva, and C.U. Segre, *Adv. Energy Mater.* **8**, 1702134 (2018).

Sn₄P₃/graphite path lengths



Sn-Sn distance close to those of metallic Sn indicate the presence of small Sn clusters which may never fully lithiate

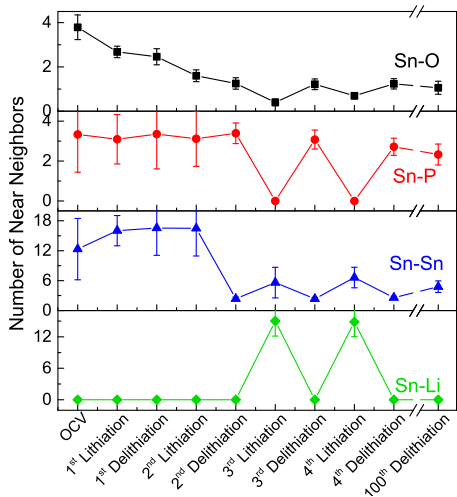
Longer Sn-P distance characteristic of Sn₄P₃ is gone after initial conversion to the SnP_x amorphous phase is complete

Only 2 Sn-Li paths present in this material

Sn-O distances remain constant, likely indicative of surface contamination

Y. Ding et al., "In situ EXAFS-derived mechanism of highly reversible tin phosphide/graphite composite anode for Li-ion batteries," Y. Ding, Z. Li, E.V. Timofeeva, and C.U. Segre, *Adv. Energy Mater.* **8**, 1702134 (2018).

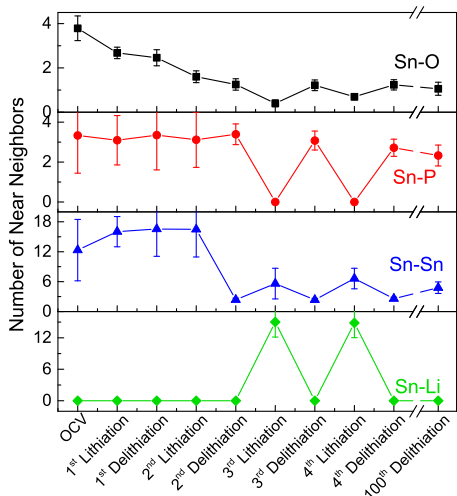
Sn₄P₃/graphite coordination numbers



Sn-O neighbors decrease quickly, remaining small and partially reversible up to 100 cycles

Y. Ding et al., "In situ EXAFS-derived mechanism of highly reversible tin phosphide/graphite composite anode for Li-ion batteries," Y. Ding, Z. Li, E.V. Timofeeva, and C.U. Segre, *Adv. Energy Mater.* **8**, 1702134 (2018).

Sn₄P₃/graphite coordination numbers

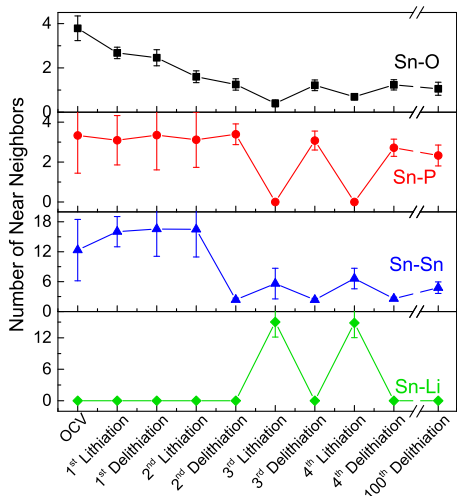


Sn-O neighbors decrease quickly, remaining small and partially reversible up to 100 cycles

Sn-P reversible after initial conversion with a slow decrease which correlates to capacity loss

Y. Ding et al., "In situ EXAFS-derived mechanism of highly reversible tin phosphide/graphite composite anode for Li-ion batteries," Y. Ding, Z. Li, E.V. Timofeeva, and C.U. Segre, *Adv. Energy Mater.* **8**, 1702134 (2018).

Sn₄P₃/graphite coordination numbers



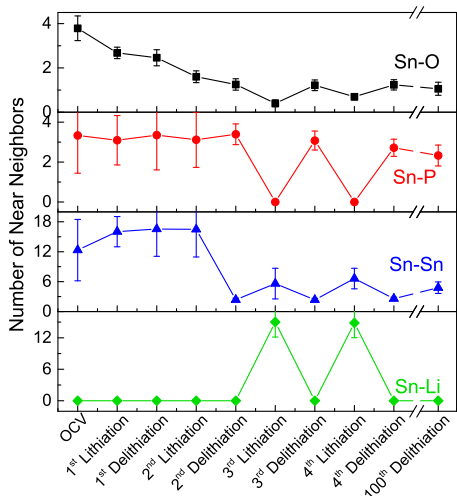
Sn-O neighbors decrease quickly, remaining small and partially reversible up to 100 cycles

Sn-P reversible after initial conversion with a slow decrease which correlates to capacity loss

Very small Sn-Sn metallic clusters present throughout

Y. Ding et al., "In situ EXAFS-derived mechanism of highly reversible tin phosphide/graphite composite anode for Li-ion batteries," Y. Ding, Z. Li, E.V. Timofeeva, and C.U. Segre, *Adv. Energy Mater.* **8**, 1702134 (2018).

Sn₄P₃/graphite coordination numbers



Sn-O neighbors decrease quickly, remaining small and partially reversible up to 100 cycles

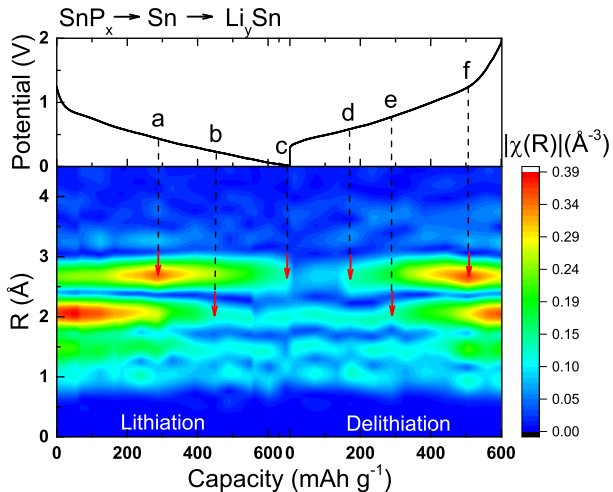
Sn-P reversible after initial conversion with a slow decrease which correlates to capacity loss

Very small Sn-Sn metallic clusters present throughout

The ~ 3.3 Sn-P neighbors in the delithiated state indicate a possibly tetrahedral Sn coordination in SnP_x

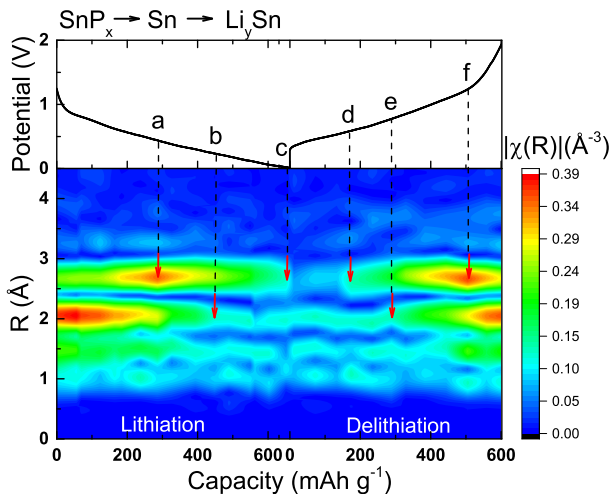
Y. Ding et al., "In situ EXAFS-derived mechanism of highly reversible tin phosphide/graphite composite anode for Li-ion batteries," Y. Ding, Z. Li, E.V. Timofeeva, and C.U. Segre, *Adv. Energy Mater.* **8**, 1702134 (2018).

Third cycle dynamic snapshot

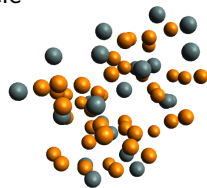


"In situ EXAFS-derived mechanism of highly reversible tin phosphide/graphite composite anode for Li-ion batteries," Y. Ding, Z. Li, E.V. Timofeeva, and C.U. Segre, *Adv. Energy Mater.* **8**, 1702134 (2018).

Third cycle dynamic snapshot

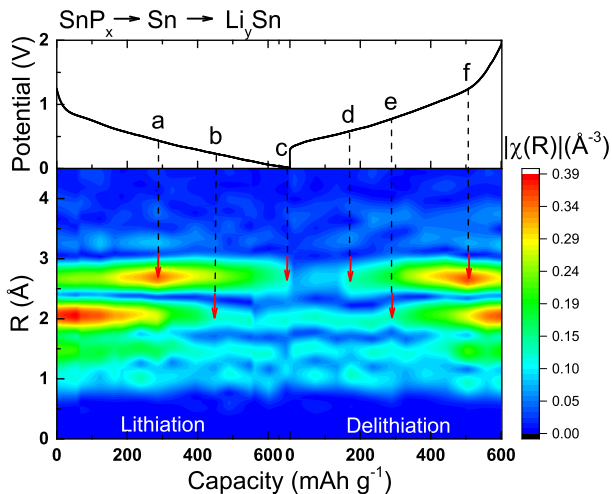


Amorphous SnP_x fully formed at start of 3rd cycle

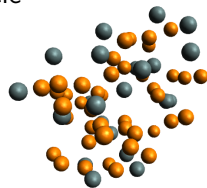


"In situ EXAFS-derived mechanism of highly reversible tin phosphide/graphite composite anode for Li-ion batteries," Y. Ding, Z. Li, E.V. Timofeeva, and C.U. Segre, *Adv. Energy Mater.* **8**, 1702134 (2018).

Third cycle dynamic snapshot



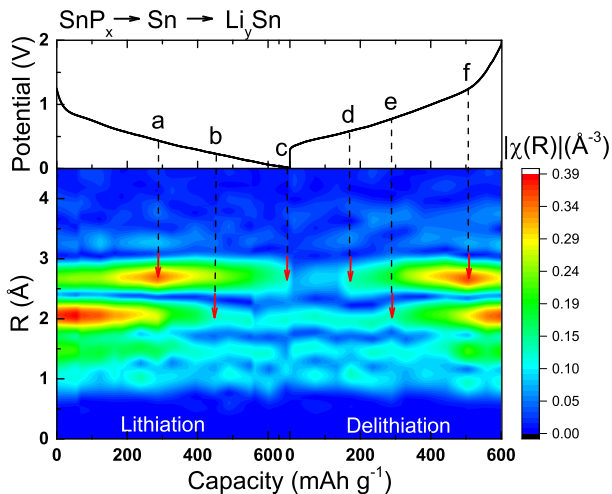
Amorphous SnP_x fully formed at start of 3rd cycle



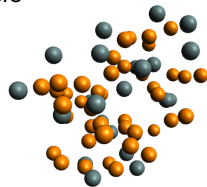
a. Sn lithiating

"In situ EXAFS-derived mechanism of highly reversible tin phosphide/graphite composite anode for Li-ion batteries," Y. Ding, Z. Li, E.V. Timofeeva, and C.U. Segre, *Adv. Energy Mater.* **8**, 1702134 (2018).

Third cycle dynamic snapshot



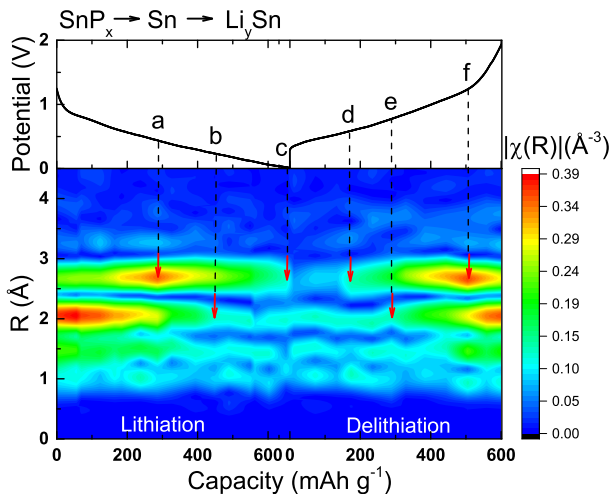
Amorphous SnP_x fully formed at start of 3rd cycle



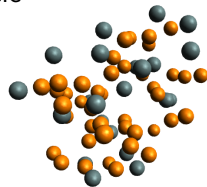
- a. Sn lithiating
- b. SnP_x all gone

"In situ EXAFS-derived mechanism of highly reversible tin phosphide/graphite composite anode for Li-ion batteries," Y. Ding, Z. Li, E.V. Timofeeva, and C.U. Segre, *Adv. Energy Mater.* **8**, 1702134 (2018).

Third cycle dynamic snapshot



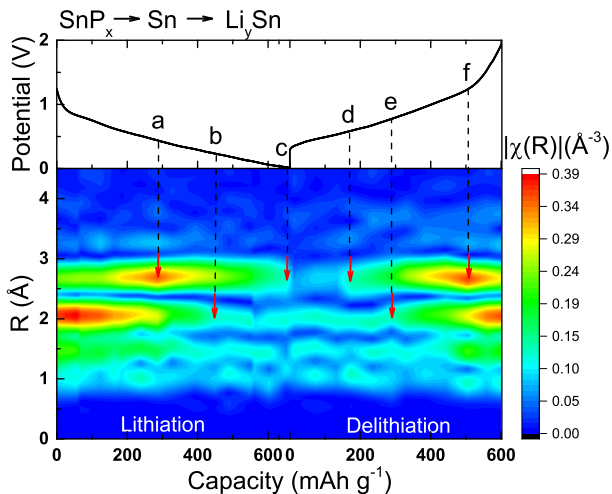
Amorphous SnP_x fully formed at start of 3rd cycle



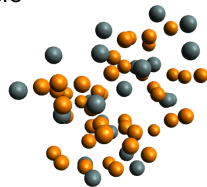
- a. Sn lithiating
- b. SnP_x all gone
- c. full lithiation

"In situ EXAFS-derived mechanism of highly reversible tin phosphide/graphite composite anode for Li-ion batteries," Y. Ding, Z. Li, E.V. Timofeeva, and C.U. Segre, *Adv. Energy Mater.* **8**, 1702134 (2018).

Third cycle dynamic snapshot



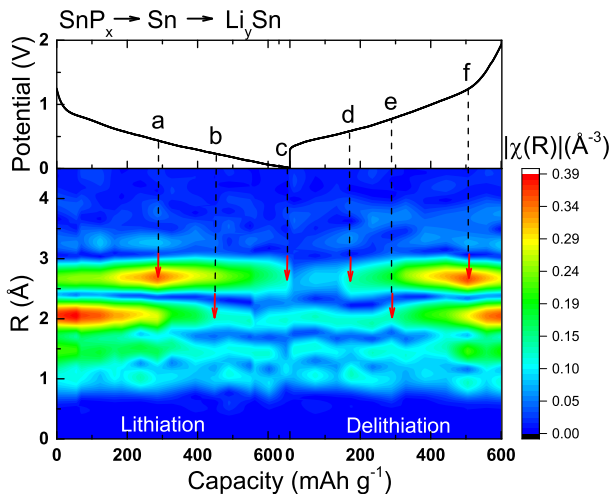
Amorphous SnP_x fully formed at start of 3rd cycle



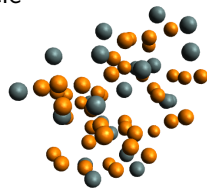
- a. Sn lithiating
- b. SnP_x all gone
- c. full lithiation
- d. Sn appears

"In situ EXAFS-derived mechanism of highly reversible tin phosphide/graphite composite anode for Li-ion batteries," Y. Ding, Z. Li, E.V. Timofeeva, and C.U. Segre, *Adv. Energy Mater.* **8**, 1702134 (2018).

Third cycle dynamic snapshot



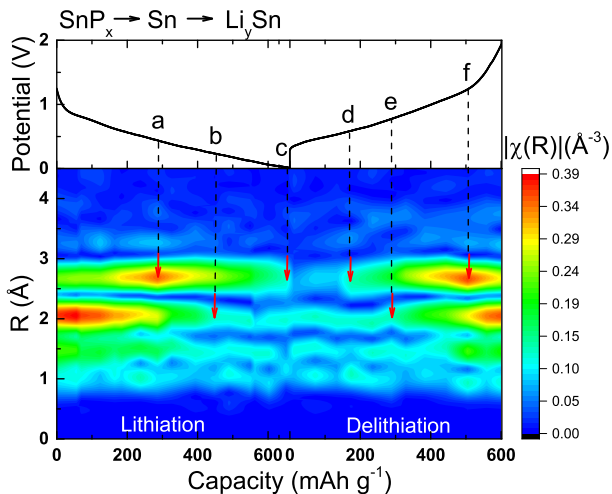
Amorphous SnP_x fully formed at start of 3rd cycle



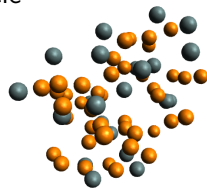
- a. Sn lithiating
- b. SnP_x all gone
- c. full lithiation
- d. Sn appears
- e. SnP_x appears

"In situ EXAFS-derived mechanism of highly reversible tin phosphide/graphite composite anode for Li-ion batteries," Y. Ding, Z. Li, E.V. Timofeeva, and C.U. Segre, *Adv. Energy Mater.* **8**, 1702134 (2018).

Third cycle dynamic snapshot



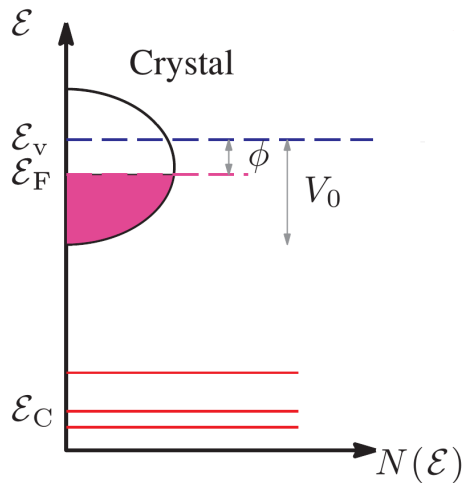
Amorphous SnP_x fully formed at start of 3rd cycle



- a. Sn lithiating
- b. SnP_x all gone
- c. full lithiation
- d. Sn appears
- e. SnP_x appears
- f. Sn delithiated

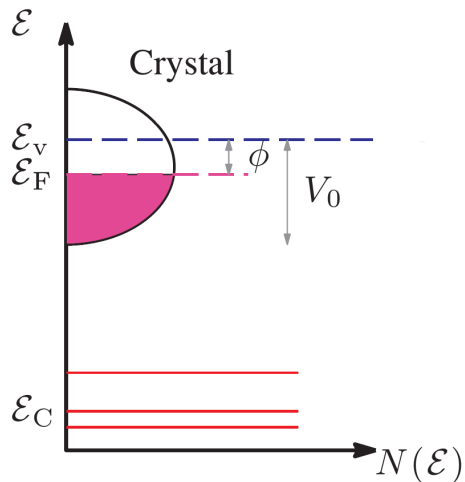
"In situ EXAFS-derived mechanism of highly reversible tin phosphide/graphite composite anode for Li-ion batteries," Y. Ding, Z. Li, E.V. Timofeeva, and C.U. Segre, *Adv. Energy Mater.* **8**, 1702134 (2018).

The photoemission process



Photoemission is the complement to XAFS. It probes the filled states below the Fermi level

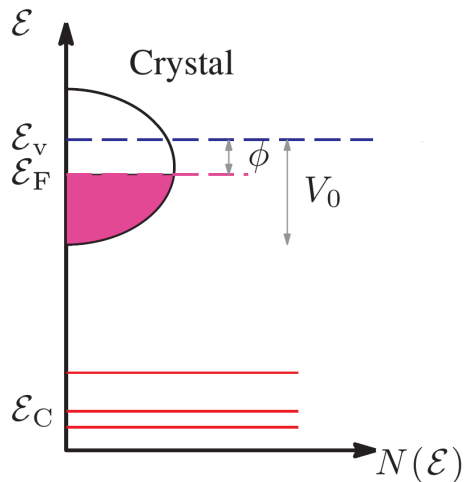
The photoemission process



Photoemission is the complement to XAFS. It probes the filled states below the Fermi level

The dispersion relation of electrons in a solid, $\mathcal{E}(\vec{q})$ can be probed by angle resolved photoemission since both the kinetic energy, \mathcal{E}_{kin} , and the angle, θ are measured

The photoemission process

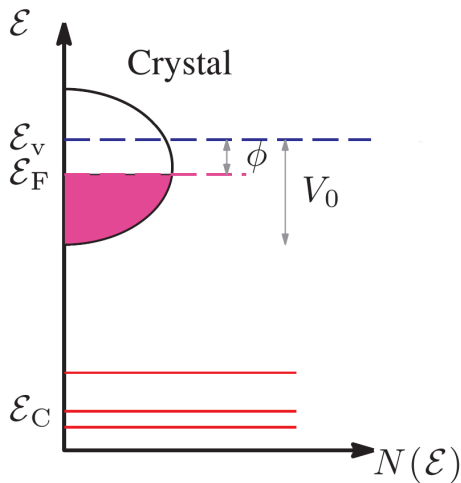


Photoemission is the complement to XAFS. It probes the filled states below the Fermi level

The dispersion relation of electrons in a solid, $\mathcal{E}(\vec{q})$ can be probed by angle resolved photoemission since both the kinetic energy, \mathcal{E}_{kin} , and the angle, θ are measured

$$\mathcal{E}_{kin}, \theta \longrightarrow \mathcal{E}(\vec{q})$$

The photoemission process



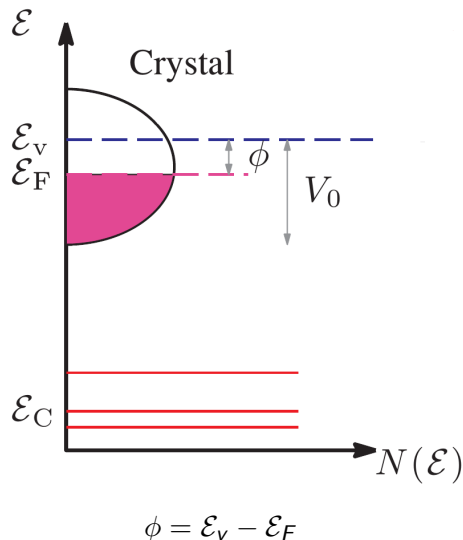
Photoemission is the complement to XAFS. It probes the filled states below the Fermi level

The dispersion relation of electrons in a solid, $\mathcal{E}(\vec{q})$ can be probed by angle resolved photoemission since both the kinetic energy, \mathcal{E}_{kin} , and the angle, θ are measured

$$\mathcal{E}_{kin}, \theta \longrightarrow \mathcal{E}(\vec{q})$$

The core levels are tightly bound at an energy ε_C below the Fermi level

The photoemission process



Photoemission is the complement to XAFS. It probes the filled states below the Fermi level

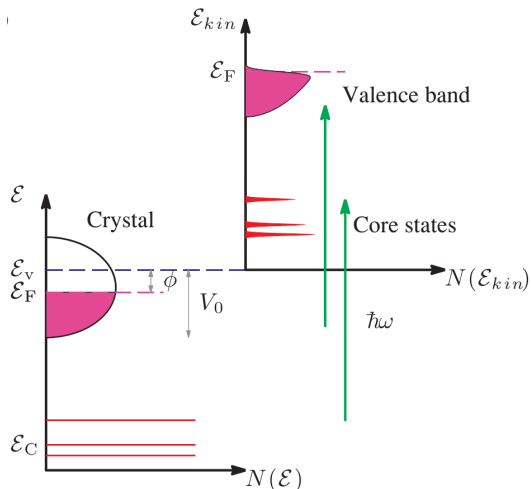
The dispersion relation of electrons in a solid, $\mathcal{E}(\vec{q})$ can be probed by angle resolved photoemission since both the kinetic energy, \mathcal{E}_{kin} , and the angle, θ are measured

$$\mathcal{E}_{kin}, \theta \rightarrow \mathcal{E}(\vec{q})$$

The core levels are tightly bound at an energy \mathcal{E}_C below the Fermi level

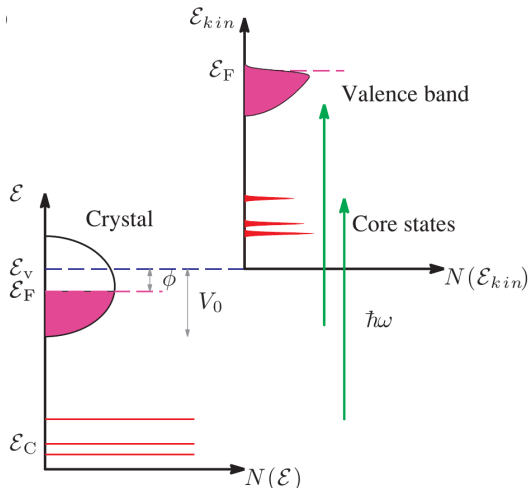
The work function, ϕ , is the minimum energy required to promote an electron from the top of the valence band at the Fermi energy, \mathcal{E}_F , to the vacuum energy, \mathcal{E}_v

The photoemission process



With the incident photon energy, $\hbar\omega$, held constant, an analyzer is used to measure the kinetic energy, \mathcal{E}_{kin} , of the photoelectrons emitted from the surface of the sample

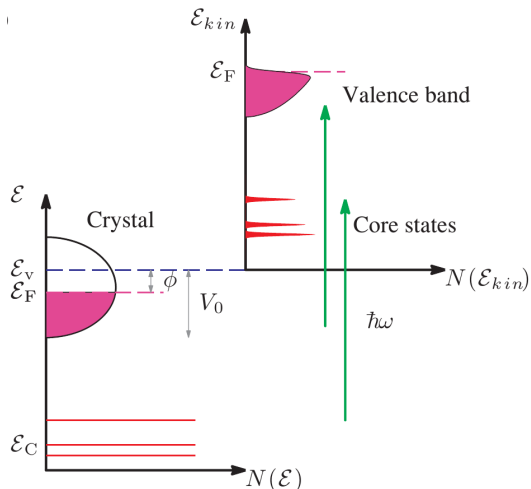
The photoemission process



With the incident photon energy, $\hbar\omega$, held constant, an analyzer is used to measure the kinetic energy, \mathcal{E}_{kin} , of the photoelectrons emitted from the surface of the sample

if \mathcal{E}_i is the initial energy of the electron, the binding energy, \mathcal{E}_B is

The photoemission process

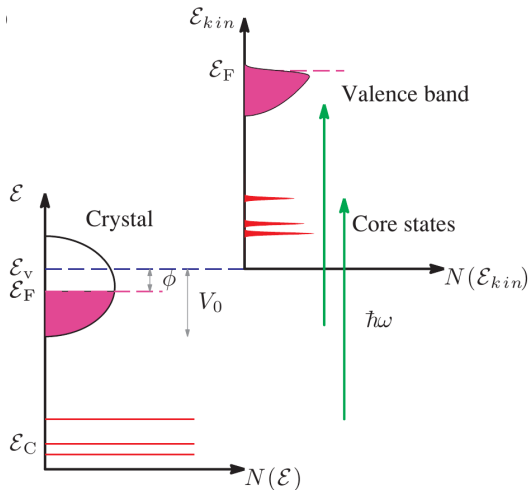


With the incident photon energy, $\hbar\omega$, held constant, an analyzer is used to measure the kinetic energy, \mathcal{E}_{kin} , of the photoelectrons emitted from the surface of the sample

if \mathcal{E}_i is the initial energy of the electron, the binding energy, \mathcal{E}_B is

$$\mathcal{E}_B = \mathcal{E}_F - \mathcal{E}_i$$

The photoemission process



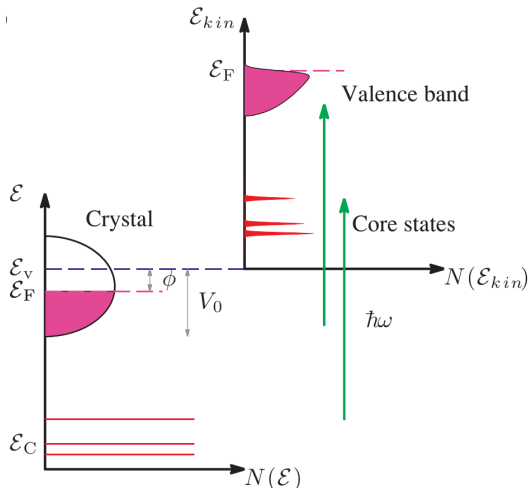
With the incident photon energy, $\hbar\omega$, held constant, an analyzer is used to measure the kinetic energy, \mathcal{E}_{kin} , of the photoelectrons emitted from the surface of the sample

if \mathcal{E}_i is the initial energy of the electron, the binding energy, \mathcal{E}_B is

$$\mathcal{E}_B = \mathcal{E}_F - \mathcal{E}_i$$

and the measured kinetic energy gives the binding energy

The photoemission process



With the incident photon energy, $\hbar\omega$, held constant, an analyzer is used to measure the kinetic energy, \mathcal{E}_{kin} , of the photoelectrons emitted from the surface of the sample

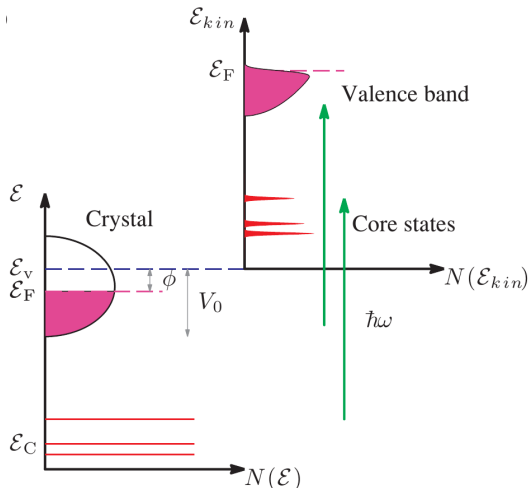
if \mathcal{E}_i is the initial energy of the electron, the binding energy, \mathcal{E}_B is

$$\mathcal{E}_B = \mathcal{E}_F - \mathcal{E}_i$$

and the measured kinetic energy gives the binding energy

$$\mathcal{E}_{kin} = \frac{\hbar^2 q_v^2}{2m}$$

The photoemission process



With the incident photon energy, $\hbar\omega$, held constant, an analyzer is used to measure the kinetic energy, \mathcal{E}_{kin} , of the photoelectrons emitted from the surface of the sample

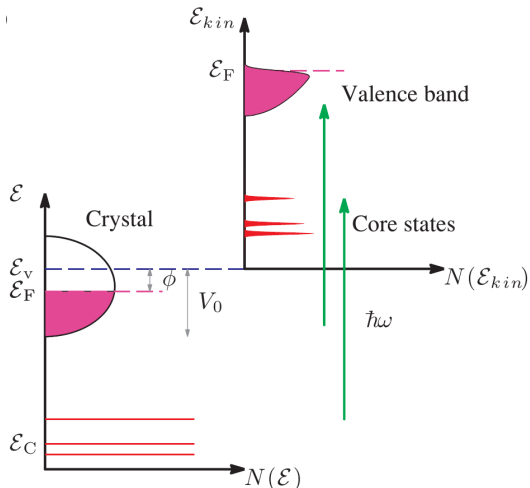
if \mathcal{E}_i is the initial energy of the electron, the binding energy, \mathcal{E}_B is

$$\mathcal{E}_B = \mathcal{E}_F - \mathcal{E}_i$$

and the measured kinetic energy gives the binding energy

$$\mathcal{E}_{kin} = \frac{\hbar^2 q_v^2}{2m} = \hbar\omega - \phi - \mathcal{E}_B$$

The photoemission process



With the incident photon energy, $\hbar\omega$, held constant, an analyzer is used to measure the kinetic energy, \mathcal{E}_{kin} , of the photoelectrons emitted from the surface of the sample

if \mathcal{E}_i is the initial energy of the electron, the binding energy, \mathcal{E}_B is

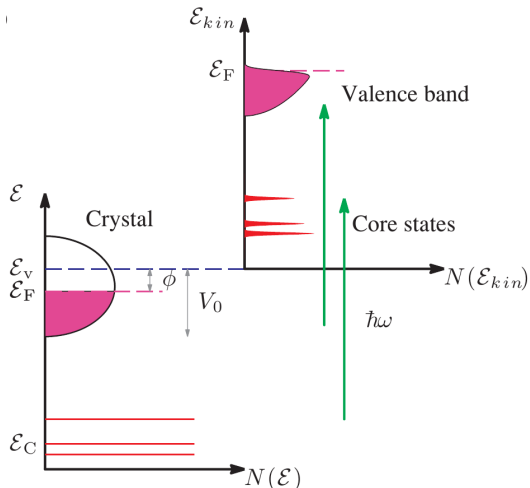
$$\mathcal{E}_B = \mathcal{E}_F - \mathcal{E}_i$$

and the measured kinetic energy gives the binding energy

$$\mathcal{E}_{kin} = \frac{\hbar^2 q_v^2}{2m} = \hbar\omega - \phi - \mathcal{E}_B$$

the maximum kinetic energy measured is thus related to the Fermi energy

The photoemission process



With the incident photon energy, $\hbar\omega$, held constant, an analyzer is used to measure the kinetic energy, \mathcal{E}_{kin} , of the photoelectrons emitted from the surface of the sample

if \mathcal{E}_i is the initial energy of the electron, the binding energy, \mathcal{E}_B is

$$\mathcal{E}_B = \mathcal{E}_F - \mathcal{E}_i$$

and the measured kinetic energy gives the binding energy

$$\mathcal{E}_{kin} = \frac{\hbar^2 q_v^2}{2m} = \hbar\omega - \phi - \mathcal{E}_B$$

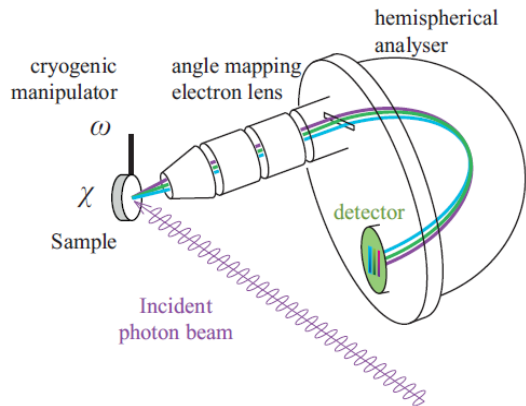
the maximum kinetic energy measured is thus related to the Fermi energy

the core states are used to fingerprint the chemical composition of the sample

Hemispherical mirror analyzer



The electric field between the two hemispheres of radius R_1 and R_2 has a R^2 dependence from the center of the hemispheres



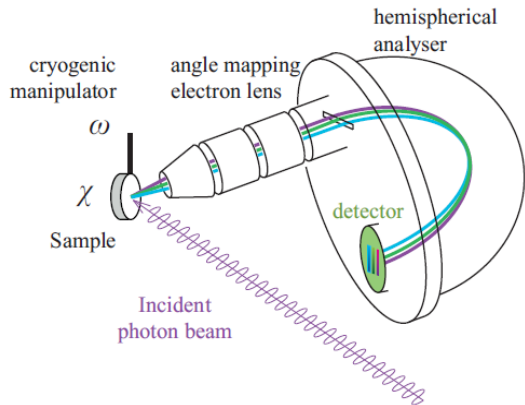
Hemispherical mirror analyzer



The electric field between the two hemispheres of radius R_1 and R_2 has a R^2 dependence from the center of the hemispheres

Electrons with \mathcal{E}_0 , called the “pass energy”, will follow a circular path of radius

$$R_0 = (R_1 + R_2)/2$$



Hemispherical mirror analyzer

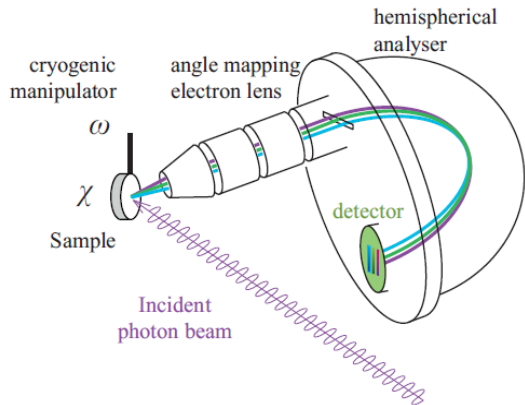


The electric field between the two hemispheres of radius R_1 and R_2 has a R^2 dependence from the center of the hemispheres

Electrons with \mathcal{E}_0 , called the “pass energy”, will follow a circular path of radius

$$R_0 = (R_1 + R_2)/2$$

Electrons with lower energy will fall inside this circular path while those with higher energy will fall outside



Hemispherical mirror analyzer



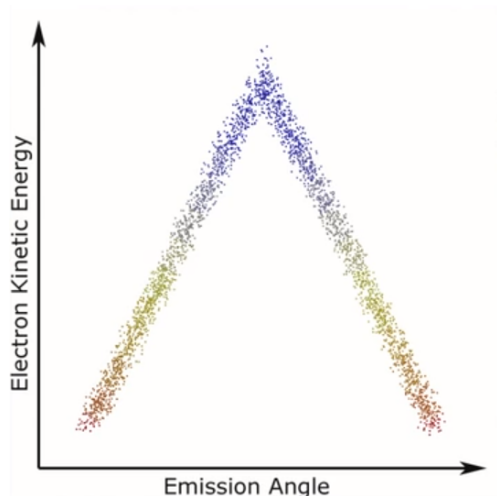
The electric field between the two hemispheres of radius R_1 and R_2 has a R^2 dependence from the center of the hemispheres

Electrons with \mathcal{E}_0 , called the “pass energy”, will follow a circular path of radius

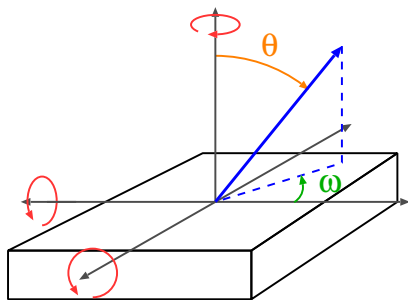
$$R_0 = (R_1 + R_2)/2$$

Electrons with lower energy will fall inside this circular path while those with higher energy will fall outside

Electrons with different azimuthal exit angles ω will map to different positions on the 2D detector



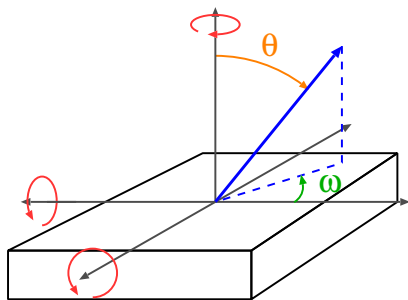
Photoelectron momentum



Photoelectron momentum



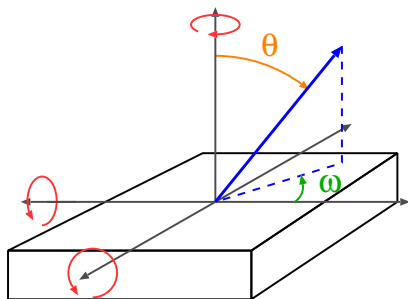
The total **momentum** of the photoelectron is calculated from the measured kinetic energy



Photoelectron momentum



The total **momentum** of the photoelectron is calculated from the measured kinetic energy



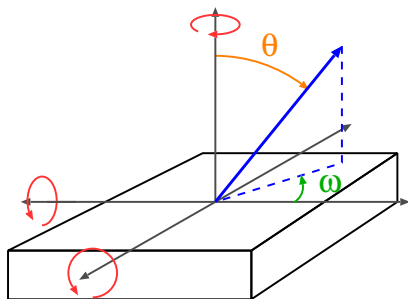
$$\hbar q_e = \sqrt{2m\mathcal{E}_{kin}}$$

Photoelectron momentum



The total **momentum** of the photoelectron is calculated from the measured kinetic energy

since the momentum of the electron parallel to the surface must be conserved, the original momentum of the electron can be computed from the **polar angle** of the sample to the detector and the **azimuthal angle** measured on the 2D detector



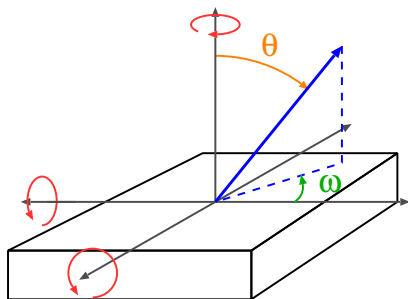
$$\hbar q_e = \sqrt{2m\mathcal{E}_{kin}}$$

Photoelectron momentum



The total **momentum** of the photoelectron is calculated from the measured kinetic energy

since the momentum of the electron parallel to the surface must be conserved, the original momentum of the electron can be computed from the **polar angle** of the sample to the detector and the **azimuthal angle** measured on the 2D detector



$$\hbar q_e = \sqrt{2m\mathcal{E}_{kin}}$$

$$\hbar q_{\parallel x} = \hbar q_e \sin \theta \cos \omega$$

$$\hbar q_{\parallel y} = \hbar q_e \sin \theta \sin \omega$$

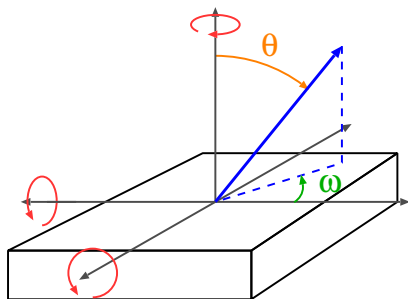
Photoelectron momentum



The total **momentum** of the photoelectron is calculated from the measured kinetic energy

since the momentum of the electron parallel to the surface must be conserved, the original momentum of the electron can be computed from the **polar angle** of the sample to the detector and the **azimuthal angle** measured on the 2D detector

the perpendicular component of the original momentum can be obtained by assuming a free electron and measuring the inner potential, V_0 at $\theta = 0$



$$\hbar q_e = \sqrt{2m\mathcal{E}_{kin}}$$

$$\hbar q_{\parallel x} = \hbar q_e \sin \theta \cos \omega$$

$$\hbar q_{\parallel y} = \hbar q_e \sin \theta \sin \omega$$

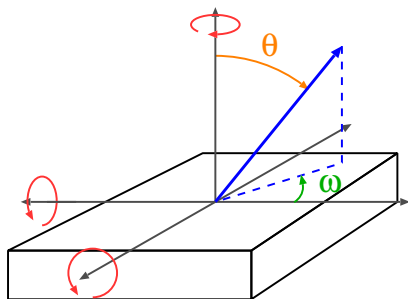
Photoelectron momentum



The total **momentum** of the photoelectron is calculated from the measured kinetic energy

since the momentum of the electron parallel to the surface must be conserved, the original momentum of the electron can be computed from the **polar angle** of the sample to the detector and the **azimuthal angle** measured on the 2D detector

the perpendicular component of the original momentum can be obtained by assuming a free electron and measuring the inner potential, V_0 at $\theta = 0$



$$\hbar q_e = \sqrt{2m\mathcal{E}_{kin}}$$

$$\hbar q_{\parallel x} = \hbar q_e \sin \theta \cos \omega$$

$$\hbar q_{\parallel y} = \hbar q_e \sin \theta \sin \omega$$

$$\hbar q_{\perp} = \sqrt{2m(\mathcal{E}_{kin} \cos^2 \theta + V_0)}$$

Photoelectron momentum

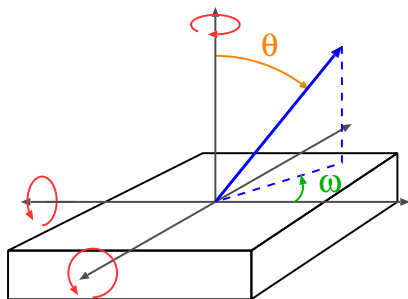


The total **momentum** of the photoelectron is calculated from the measured kinetic energy

since the momentum of the electron parallel to the surface must be conserved, the original momentum of the electron can be computed from the **polar angle** of the sample to the detector and the **azimuthal angle** measured on the 2D detector

the perpendicular component of the original momentum can be obtained by assuming a free electron and measuring the inner potential, V_0 at $\theta = 0$

the electron dispersion curve can be fully mapped by sample **rotations**



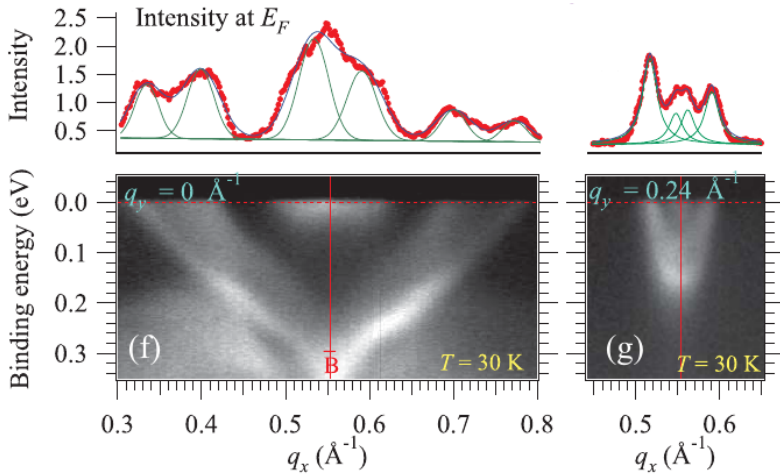
$$\hbar q_e = \sqrt{2m\mathcal{E}_{kin}}$$

$$\hbar q_{\parallel x} = \hbar q_e \sin \theta \cos \omega$$

$$\hbar q_{\parallel y} = \hbar q_e \sin \theta \sin \omega$$

$$\hbar q_{\perp} = \sqrt{2m(\mathcal{E}_{kin} \cos^2 \theta + V_0)}$$

ARPES experimental data





Photoemission spectroscopy is generally used for surface sensitive measurements because of the low energy of the incident photons (< 2 keV)

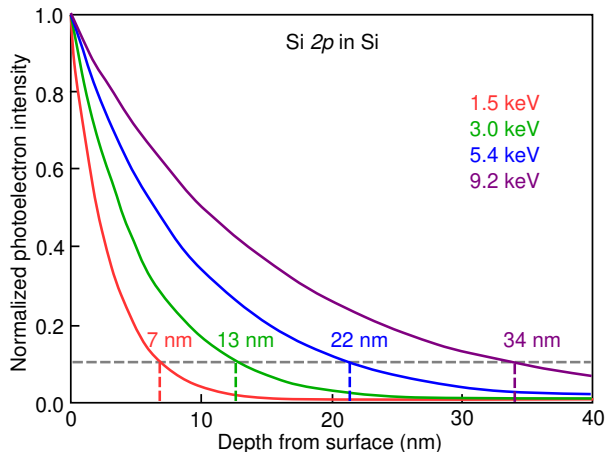


Photoemission spectroscopy is generally used for surface sensitive measurements because of the low energy of the incident photons (< 2 keV)

High energy synchrotrons offer the opportunity to use hard x-ray photoelectron spectroscopy (HAXPES)



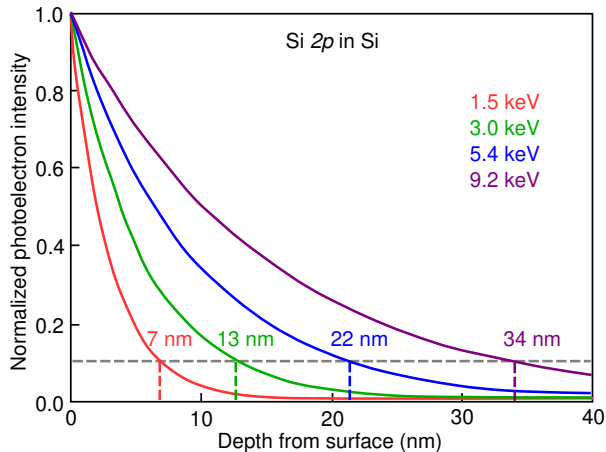
Photoemission spectroscopy is generally used for surface sensitive measurements because of the low energy of the incident photons (< 2 keV)



High energy synchrotrons offer the opportunity to use hard x-ray photoelectron spectroscopy (HAXPES)



Photoemission spectroscopy is generally used for surface sensitive measurements because of the low energy of the incident photons (< 2 keV)

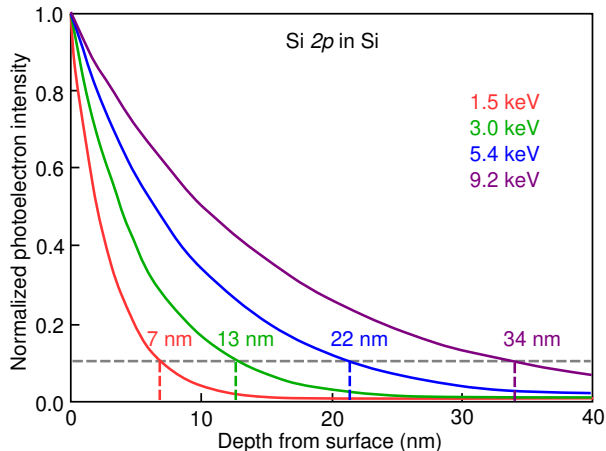


High energy synchrotrons offer the opportunity to use hard x-ray photoelectron spectroscopy (HAXPES)

HAXPES advantages include



Photoemission spectroscopy is generally used for surface sensitive measurements because of the low energy of the incident photons (< 2 keV)



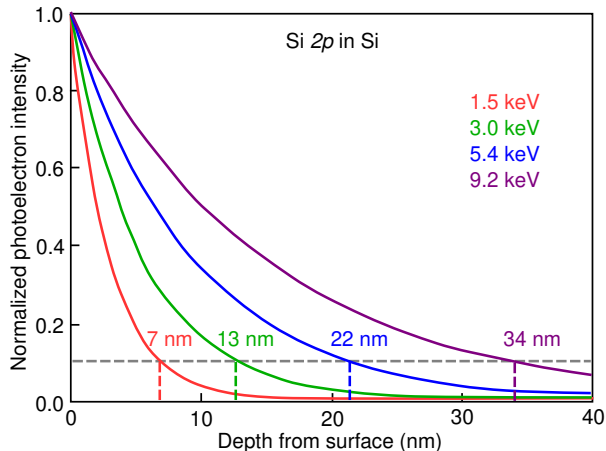
High energy synchrotrons offer the opportunity to use hard x-ray photoelectron spectroscopy (HAXPES)

HAXPES advantages include

measurement of K edges of 3d elements, L edges of 5d elements, and M edges of 5f elements



Photoemission spectroscopy is generally used for surface sensitive measurements because of the low energy of the incident photons (< 2 keV)



High energy synchrotrons offer the opportunity to use hard x-ray photoelectron spectroscopy (HAXPES)

HAXPES advantages include

measurement of K edges of 3d elements, L edges of 5d elements, and M edges of 5f elements

ability to measure bulk photoemission and buried interfaces as well as the surface